TAMPEREEN TEKNILLINEN YLIOPISTO
TAMPERE UNIVERSITY OF TECHNOLOGY
Julkaisu 724 • Publication 724

Antti Härkönen

Optically-Pumped Semiconductor Disk Lasers for Generating Visible and Infrared Radiation

Tampere 2008

Tampereen teknillinen yliopisto. Julkaisu 724
Tampere University of Technology. Publication 724

Antti Härkönen

Optically-Pumped Semiconductor Disk Lasers for Generating Visible and Infrared Radiation

Thesis for the degree of Doctor of Technology to be presented with due permission for public examination and criticism in Tietotalo Building, Auditorium TB111, at Tampere University of Technology, on the 27th of March 2008, at 12 noon.

Tampereen teknillinen yliopisto - Tampere University of Technology
Tampere 2008

ISBN 978-952-15-1941-3 (printed)
ISBN 978-952-15-2017-4 (PDF)
ISSN 1459-2045

Abstract

Optically-pumped semiconductor disk lasers are light sources that combine traditional solid state disk laser architecture with gain material made of semiconductor nano-layers. The laser design offers an attractive oppportunity to produce high-power, high-brightness laser radiation at a wavelength that is controlled by semiconductor bandgap engineering. Moreover, the laser can be very compact, yet it can be mode-locked to produce ultra-short optical pulses or efficiently frequency-doubled to produce visible colors. Because of their advantageous characteristics, semiconductor disk lasers are highly interesting for a number of applications including laser projection, optical pumping, optical clocking and substitution of certain gas- and ion-lasers.

This thesis concerns the research and development of semiconductor disk lasers emitting at visible and infrared wavelengths. The semiconductor structures used in this work are based on InGaAs/GaAs, GaInNAs/GaAs and GaInSb/GaSb material systems. In particular, it was shown in this thesis that frequency-doubled dilute nitride GaInNAs disk lasers can be used to generate the high-power red emission that is preferred for display applications. Power scaling to the 1-W level and 100 nm wavelength tunability were demonstrated for a gallium antimonide based disk laser operating near 2 μm. The novel concept of an intracavity frequency-mixed dual-wavelength disk laser was proposed and demonstrated in this thesis. The laser, operating at two infrared wavelengths near 1 μm, generated 130 mW of aquamarine sum-frequency emission in total, suggesting good spatial and temporal overlap of the two near-infrared beams. Based on this observation it is reasonable to believe that efficient difference-frequency generation producing coherent emission at a mid-infrared wavelength could be possible in a similar laser in the future.

Preface

This thesis contains some essential parts of the work that I have carried out at the Optoelectronics Research Centre, Tampere University of Technology, during the years 2004–2007, under the supervision of professor Oleg G. Okhotnikov. At the starting point I had no experience in building lasers, nor did I have the funding for it. Therefore, I want to thank Jari Näppi for helping me to build the very first laser and *Jenny ja Antti Wihurin rahasto* for the financial support that enabled us to start the research program. Later on this work has also been supported financially by the *National Graduate School in Nanosciences*, *Nokia Oyj:n säätiö*, *Emil Aaltosen säätiö*, the *European Commission* and *Tekes*, which I would like to acknowledge.

During the course of this project I have relied on the support and kind help of friends and colleagues to whom I'd like to present my gratitude. All semiconductor crystals exploited in this work were fabricated by Soile Suomalainen, Tomi Leinonen, Janne Konttinen, Pietari Tuomisto, Jari Lyytikäinen and Karl Rößner. I want to thank you all for spending the long hours at the MBE and being the best colleagues one could ask for. In processing related issues I have relied on the vast knowledge and experience of Pirjo Leinonen, Jukka Viheriälä and Ilkka Hirvonen, who initially introduced me to the the field of semiconductor device fabrication. Thanks for taking the time! I would like to thank my colleagues Jussi Rautiainen and Esa Saarinen for substantial contribution to collecting data with high accuracy and reliability, and also for being the key players in ORC's floorball team. I do owe you one!

I also want to thank my co-workers Matei, Antti I., Robert, Dionisio, Samuli, Tommi and Juho, it has been an honor and pleasure to work with you. I want to credit my best friend Lasse Orsila for his dedicated work in designing and fabricating all thin-film

structures used throughout this work, solving various computer and LaTeX-related issues and putting up with my taste of music year in, year out. On a personal level I want to thank you and Reetta for the time that you have spent with us - Thanks!

I thank professor Markus Pessa for giving me the opportunity to work at ORC and supporting students with new ideas and innovations. I have really enjoyed these years and the atmosphere of enthusiasm, generosity, and the attitude of giving 100%, whether it comes to work or football. For the very same reasons I would like to thank my colleague Mircea Guina, who has also managed the funding for this work and provided many of the ideas used in this thesis.

The lasers presented here would not have been built without numerous custom made metal components, sometimes machined to micrometer accuracy by Timo Lindqvist and Bengt Holmström, so cheers for that! I must also thank Anne Viherkoski and Kerttu Hokkanen for herding a group of 70 researchers and assistants, plus taking care of all the administrative business and financial issues simultaneously. When it comes to nonlinear optics I would like to acknowledge valuable help from professor Martti Kauranen, who has deep insight in the field and extraordinary skills in teaching the subject. A special thanks for help in language related issues goes to Charis Reith and Steve Busick.

Last but not least, want to give a big hug to my wife Aino, and my family for the long term support. Thank you!

Tampere, February 2008
Antti Härkönen

Contents

List of Publications

This thesis is a compendium, which contains some unpublished material, but is mainly based on the following papers published in open literature.

[P1] A. Härkönen, S. Suomalainen, E. Saarinen, L. Orsila, R. Koskinen, O. G. Okhotnikov, S. Calvez and M. Dawson, "4 W single-transverse mode VECSEL utilising intra-cavity diamond heat spreader," *IEE Electronics Letters*, vol. 42, no. 12, pp. 693–694, 2006.

[P2] A. Härkönen, J. Rautiainen, M. Guina, J. Konttinen, P. Tuomisto, L. Orsila, M. Pessa and O. G. Okhotnikov, "High power frequency doubled GaInNAs semiconductor disk laser emitting at 615 nm," *Optics Express*, vol. 15, no. 6, pp. 3224–3229, 2007.

[P3] A. Härkönen, M. Guina, O. G. Okhotnikov, K. Rößner, M. Hümmer, T. Lehnhardt, M. Müller, A. Forchel and M. Fischer, "1-W antimonide-based vertical external cavity surface emitting laser operating at 2-μm," *Optics Express*, vol. 14, no. 14, pp. 6479–6484, 2006.

[P4] A. Härkönen, M. Guina, K. Rößner, M. Hümmer, T. Lehnhardt, M. Müller, A. Forchel, M. Fischer, J. Koeth and O. G. Okhotnikov, "Tunable self-seeded semiconductor disk laser operating at 2 μm," *IET Electronics Letters*, vol. 43, no. 8, pp. 457–458, 2007.

[P5] A. Härkönen, J. Rautiainen, T. Leinonen, Y. A. Morozov, L. Orsila, M. Guina, M. Pessa and O. G. Okhotnikov, "Intracavity sum-frequency generation in dual-wavelength semiconductor disk laser," *IEEE Photonics Technology Letters*, vol. 19, no. 19, pp. 1550–1552, 2007.

Supplementary publications

Other publications related to this work, but not included in this thesis:

[S1] A. Härkönen, J. Rautiainen, J. Konttinen, T. Leinonen, P. Tuomisto, L. Orsila, M. Guina, M. Pessa and O. G. Okhotnikov, "Optically-pumped semiconductor disk lasers for second-harmonic and sum-frequency generation" in *Proceedings of OSA Nonlinear Optics: Materials, Fundamentals and Applications (NLO)*, Kona, USA, July 30, 2007, paper FB6

[S2] A. Härkönen, T. Jouhti, N. V. Tkachenko, H. Lemmetyinen, B. Ryvkin, O. G. Okhotnikov, T. Sajavaara and J. Keinonen, "Dynamics of photoluminescence in GaInNAs saturable absorber mirrors," *Applied Physics A*, vol. 77, pp. 861–863, 2003.

[S3] E. J. Saarinen, A. Härkönen, R. Herda, S. Suomalainen, L. Orsila, T. Hakulinen, M. Guina and O. G. Okhotnikov, "Harmonically mode-locked VECSELs for multi-GHz pulse train generation," *Optics Express*, vol. 15, no. 3, pp. 955–964, 2007.

[S4] J. Konttinen, A. Härkönen, P. Tuomisto, M. Guina, J. Rautiainen, M. Pessa and O. G. Okhotnikov, "High-power (>1W) dilute nitride semiconductor disk laser emitting at 1240 nm," *New Journal of Physics*, vol. 9, no. 5, p. 140, 2007.

[S5] J. Rautiainen, A. Härkönen, V.-M. Korpijärvi, P. Tuomisto, M. Guina and O. G. Okhotnikov, "2.7 W tunable orange-red GaInNAs semiconductor disk laser," *Optics Express*, vol. 15, no. 26, pp. 18345–18350, 2007.

[S6] J. Rautiainen, A. Härkönen, P. Tuomisto, J. Konttinen, L. Orsila, M. Guina and O. G. Okhotnikov, "1 W at 617 nm generation by intracavity frequency conversion in semiconductor disk laser," *IET Electronics Letters*, vol. 43, no. 18, pp. 980–981, 2007.

[S7] E. J. Saarinen, A. Härkönen, S. Suomalainen and O. G. Okhotnikov, "Power scalable semiconductor disk laser using multiple gain cavity," *Optics Express*, vol. 14, no. 26, pp. 12868–12871, 2006.

[S8] T. Leinonen, Y. Morozov, A. Härkönen and M. Pessa, "Vertical external-cavity surface-emitting laser for dual-wavelength generation," *IEEE Photonics Technology Letters*, vol. 17, no. 12, pp. 2508–2510, 2005.

[S9] Y. A. Morozov, T. Leinonen, A. Härkönen and M. Pessa, "Simultaneous dual-wavelength emission from vertical external-cavity surface-emitting laser: a numerical modeling," *IEEE Journal of Quantum Electronics*, vol. 42, no. 10, pp. 1055–1061, 2006.

[S10] M. Guina, A. Vainionpää, A. Härkönen, L. Orsila, J. Lyytikäinen and O. G. Okhotnikov, "Vertical-cavity saturable-absorber intensity modulator," *Optics Letters*, vol. 28, no. 1, pp. 43–45, 2003.

Author's contribution

The work presented in this thesis is a result of teamwork involving semiconductor crystal growing, semiconductor wafer characterization, sample processing, laser characterization and theoretical simulations. One part of my work was to develop suitable processing and mounting procedures for devices using intra-cavity diamond heat spreader elements and for flip-chip bonded devices using indium and AuSn solder. The second part of my work was to develop suitable characterization methods for the lasers. This work involved designing and building of laser and measurement setups, acquiring data and taking part in reporting on the results. To some extent I have also been involved in designing the gain structures.

List of Abbreviations and Symbols

AC	Alternating current
Al	Aluminium
AlAs	Aluminium arsenide
AlGaAs	Aluminium gallium arsenide
AlGaSb	Aluminium gallium antimonide
AR	Antireflective
As	Arsenic
Au	Gold
BBO	Beta-barium borate, β-BaB_2O_4
BF	Birefringent filter
CTE	Coefficient of thermal expansion
cw	Continuous wave
DBR	Distributed Bragg reflector
DFG	Difference-frequency generation
DPSSL	Diode-pumped solid state laser
EDFA	Erbium-doped fiber amplifier
ELO	Epitaxial lift-off
EP-VECSEL	Electrically-pumped vertical-external-cavity surface-emitting laser
Er	Erbium
FP	Fabry–Pérot
FSR	Free spectral range
FWHM	Full width at half maximum

Ga	Gallium
GaAs	Gallium arsenide
GaInNAs	Gallium indium nitride arsenide
GaN	Gallium nitride
GaSb	Gallium antimonide
GRIN	Graded index
HCl	Hydrochloric acid
HfO_2	Hafnium dioxide
H_2O_2	Hydrogen peroxide
Ho:YAG	Holmium-doped yttrium-aluminium-garnet
HR	High reflective
In	Indium
InGaAs	Indium gallium arsenide
InGaAsP	Indium gallium arsenide phosphide
InGaP	Indium gallium phosphide
InP	Indium phosphide
IR	Infrared
LBO	Lithium triborate, LiB_3O_5
LIDAR	Light detection and ranging
MBE	Molecular beam epitaxy
MIR	Mid-infrared
MQW	Multiple quantum wells
Nd:YAG	Neodymium-doped yttrium-aluminium-garnet
NH_4OH	Ammonium hydroxide
OC	Output coupler
OPO	Optical parametric oscillator
OP-SDL	Optically-pumped semiconductor disk laser

OPS-VECSEL	Optically-pumped-semiconductor vertical-external-cavity surface-emitting laser
ORC	Optoelectronics research centre
OSA	Optical spectrum analyzer
P	Phosphorus
PL	Photoluminescence
QD	Quantum dot
QW	Quantum well
Ra	Average roughness, average height of the bumps on a surface
RF	Radio frequency
RGB	Red-green-blue
RIE	Reactive ion etching
RoC	Radius of curvature
RPG	Resonant periodic gain
SDL	Semiconductor disk laser
SEM	Scanning electron microscope
Sb	Antimony
SESAM	Semiconductor saturable absorber mirror
SFG	Sum-frequency generation
SHG	Second-harmonic generation
SiC	Silicon carbide
SiO_2	Silicon dioxide
SMF	Single-mode fiber
SOA	Semiconductor optical amplifier
TEM	Transverse electric and magnetic
TiO_2	Titanium dioxide
UV	Ultraviolet
VBG	Volume Bragg grating

VCSEL	Vertical-cavity surface-emitting laser
VECSEL	Vertical-external-cavity surface-emitting laser
WDM	Wavelength division multiplexing

Symbols, Greek alphabet

$\Delta\lambda_{\mathrm{FSR}}$	Free spectral range in wavelength domain
$\Delta\lambda_{99\%}$	Bandwidth of $R \geq 99\%$ reflectivity band
Δn	Refractive index contrast, $\Delta n = n_H - n_L$
ε	Permittivity
θ	Propagation angle
φ	Propagation angle
λ	Wavelength
λ_B	Bragg wavelength
λ_L	Long wavelength in a dual-wavelength laser
λ_S	Short wavelength in a dual-wavelength laser
ω	Optical frequency
χ	Susceptibility

Symbols, other

A	Area
D	Distance
E	Electric field
I	Intensity
L	Length
M^2	Beam quality factor

N	Number of DBR layer pairs, $N = 1, 2, 3, \ldots$
P	Optical power, material polarization
Q	Quality factor of a laser cavity
R	Reflectivity
T	Optical transmission, Temperature
c	Speed of light in vacuum
$c.c.$	Complex conjugate
d	Thickness, nonlinear coefficient
d_{eff}	Effective nonlinear coefficient
k	Wave propagation constant
n	Refractive index
n_H	Refractive index of high index layer
n_L	Refractive index of low index layer
n_S	Refractive index of substrate
n_i	Refractive index of surrounding medium
t	Time
w_0	Beam waist radius
z	Distance along optical axis
z_R	Rayleigh range, also called Rayleigh distance

Chapter 1

Introduction

The work presented in this thesis focuses on a particular type of laser commonly known as the *optically-pumped semiconductor disk laser* (OP-SDL) or the OPS-VECSEL, (*optically-pumped-semiconductor vertical-external-cavity surface-emitting laser*). Although derived from different origins, both terms can be well justified and capture the essence of the laser's nature: that is to use optically-pumped thin-disk semiconductor gain material for generating surface-normal laser radiation in a cavity that is formed between the gain mirror and one or more laser mirrors, external to the gain structure.

The term SDL is originally derived from solid-state disk lasers, while VECSEL originates from *vertical-cavity surface-emitting lasers* (VCSELs) utilizing an external cavity. Today both terms are used interchangeably for optically-pumped devices. Vertical-external-cavity diode lasers are usually called electrically-pumped VECSELs or injection pumped VECSELs. This thesis concerns only optically-pumped devices, for which the term SDL shall be used hereinafter.

Owing to the external mirrors, SDLs are less compact than monolithic VCSELs or edge-emitting semiconductor diode lasers, such as those commonly used in DVD players, bar code readers and telecom applications. However, due to their small mode area, VCSELs or single-mode edge-emitting lasers can not typically reach the multi-watt power levels required for many industrial, medical, scientific and measurement related applications. Such applications have long been dominated by solid state, gas and ion lasers, which are in fact brightness converters; pumped with low brightness light from

multi-mode diode bars or flash pumps, these lasers can produce high power, circular single-transversal-mode output beams, required for demanding applications. Limitations to these lasers typically arise from their price, size, complexity, and efficiency in converting pump radiation into signal. Accessible spectral regions are also limited by the availability of gain materials having the required laser transitions.

The architecture of OP-SDLs is a composite of solid state disk laser geometry and semiconductor gain material. Consequently, SDLs combine many of the good features associated with solid state disk lasers with the flexibility offered by the semiconductor gain material. Contrary to VCSELs and edge-emitting lasers, the SDL cavity design allows for up-scaling of the fundamental mode area, enabling power to be extracted from a large gain area. Therefore, SDLs are capable of producing multi-watt output power with excellent beam quality, while maintaining a power density below the material damage threshold. SDLs can be highly efficient, and they can be packaged in compact form. An advantage of semiconductor gain material is mature fabrication technology and capability to cover a wide spectral range simply by controlling the material composition.

1.1 Incentives

This work was started in 2004 and it initially aimed to develop an ultra-fast multi-GHz disk laser for telecom clocking applications. Mode-locked SDLs are part of the work that was carried out during the past years, but the work included in this thesis concentrates on *continuous wave* (cw) devices and concepts that aim to broaden the spectral coverage of semiconductor disk laser technology.

It was observed at an early stage that *infrared* (IR) SDLs possess high potential for generating frequency-doubled *red-green-blue* (RGB) emission in a compact form factor. In particular, laser projection TVs and projection displays integrated in portable devices, such as laptops, would gain from compact low-cost RGB sources. Advances in the development of GaN lasers have brought blue laser diodes into the market, but so far it has been challenging to directly generate green or short wavelength (<635 nm) red emission preferred for display applications. The intracavity frequency-doubling technique has been previously applied to SDLs resulting in demonstrations of multi-watt blue [1],

green [2], and yellow [3] sources. However, when this work began, frequency-doubled amber-orange-red SDLs had not been studied extensively, and development of a high power $\sim$ 620 nm emitting GaInNAs-based SDL became one of the main objectives of this work. This part of the work is presented in chapter 4.

Another important part of this work was carried out in co-operation with Universität Würzburg in Germany, and was dedicated to GaSb-based SDLs emitting at 2-μm wavelength. Radiation in this wavelength range can be utilized in gas sensing, life sciences, and environmental monitoring. As an extension of earlier demonstrations of long wavelength GaSb-based SDLs, our aim was to further improve these devices in terms of output power and wavelength tuning. The results obtained from the 2-μm laser are described in chapter 5.

The unique feature that differentiates SDLs from conventional disk lasers is that the emission wavelength can be accurately controlled by means of bandgap engineering. This property allowed us to introduce previously an SDL that operated simultaneously at two wavelengths with large spectral separation [S8]. Within this thesis the concept was further developed and we demonstrated an intracavity frequency-mixed dual-wavelength SDL generating sum-frequency emission near 507 nm. This study aimed to set the basis for future development of a disk laser generating difference-frequency emission in the mid-infrared. The sum-frequency experiment and results are discussed in chapter 6.

This thesis is a compilation of separate pieces of the author's work in the field. A common denominator for all parts of the work is the concept of an optically-pumped thin disk semiconductor laser. The following chapters should introduce the reader to the laser concept, present previous achievements in the field and provide an overview of the author's contribution. Concluding remarks of the work are given in chapter 7.

Chapter 2

Semiconductor disk lasers

2.1 The prior art

To the author's knowledge the very first reports on an optically-pumped semiconductor disk laser were published in 1991 by W. B. Jiang et al. [4] from NTT Basic Research Laboratories and Le et al. [5] from MIT. The laser reported by NTT was based on the InP material system and emitted 190 mW near 1.5 μm wavelength. The laser was cooled with liquid nitrogen and pumped by 1.32 μm radiation from a Nd:YAG laser. Sub-picosecond pulses were reported in synchronously pumped mode-locked configuration with subsequent external pulse compression. During the very same year the group reported pulse compression down to 21 fs [6]. In 1992, low power, room temperature operation of a GaAs-based SDL in continuous wave mode and pulsed operation was reported in [7] and the NTT group reported on the first high power (700 mW) device based on GaAs material system [8].

The early reports on OP-SDLs presented truly heroic results, both in terms of continuous wave output power and ultra-short pulse generation. However, these devices were pumped with expensive solid-state or dye lasers and could not reach significant power levels at room temperature, or temperatures accessible with thermo-electric coolers, which made them unsuitable sources for practical applications.

2.2 The state of the art

The first optically-pumped semiconductor disk laser with modern design and functionality was reported in 1997 by Mark Kuznetsov et al. [9]. The laser could operate at room temperature and above, it produced relatively high output power (>0.5 W) and it was pumped with a commercial multi-mode 808-nm diode laser. These advances were made possible by development of the pump diodes, use of highly efficient multiple quantum well InGaAs/GaAs gain material and careful thermal management, which included flip-chip bonding of the sample onto a diamond heat spreader and subsequent removal of the semiconductor substrate. The combination of efficient gain material, good thermal dissipation and a practical pumping scheme has remained the design guideline for modern SDLs targeting higher power, efficiency, wide spectral coverage, passive and active mode-locking and frequency-conversion.

The output power of an SDL can be increased to many Watts with reasonable beam quality by enlarging the pumped gain area and the fundamental mode size accordingly, as demonstrated by Lutgen et al. [10] and Chilla et al. [11]. A large pump area allows an increase in pump power without risk of catastrophic optical damage, but eventually thermal roll-over and the appearance of multiple transversal-modes due to thermal lensing start to degrade the laser performance. Power scaling and distribution of the heat load by exploiting multiple gain elements is a technique that allowed earlier demonstration of a 1-kW solid state disk laser [12]. This technique was already proposed for SDLs in 1991 [5], and was later successfully demonstrated by a number of groups [13–15]. The local heat load can also be reduced by division of the pump energy into multiple spots on a single gain element as proposed in [16]. This approach is particularly suitable for micro-chip SDLs that can support operation of separate lasers sharing a single gain chip as presented in [17].

The cornerstone of SDL research has been InGaAs/GaAs-based devices emitting near 1 μm. The rapid progress in this spectral region has been due to efficient gain materials, availability of 808-nm pump diodes and the capability to grow lattice matched AlAs/GaAs Bragg reflectors on GaAs with reasonable index contrast. Lately, there has been much interest in expanding the SDL technology to spectral regions such as the blue [18], red [19, 20], 850 nm [21–23], 920 nm [24], 1100–1350 nm [25, 26], 1550 nm

[27–29] and beyond 2 μm [30, 31]. The work presented here was largely motivated by the need to broaden the spectral coverage of SDLs with high output power, especially at 580–630 nm and 2 μm. Taking into account the possibility for efficient frequency-doubling, today SDL technology can largely cover the spectral band from the ultraviolet to the long-wavelength edge of the near-infrared region, as shown in Table 2.1.

The external cavity allows use of low-loss wavelength selective elements, such as *birefringent filters* (BFs), *volume Bragg gratings* (VBGs) and *Fabry–Pérot* (FP) etalons. These elements can be effectively used to produce wavelength stabilized narrow band [32], single-frequency [33,34] and wavelength tunable radiation [35], for enhanced spectral characteristics.

In addition to spectrally selective elements, components for short pulse generation may also be included in the cavity. The broad gain bandwidth makes SDLs attractive sources for ultra-short pulse generation with potential applications in high-speed communications, switching, sampling and clocking applications. Mode-locked SDLs [39] have shown capability for producing sub-picosecond pulses [40], tens of gigahertz repetition rates [41] and high power [42]. Current semiconductor technology allows for monolithic integration of the gain mirror and the *semiconductor saturable absorber mirror* (SESAM) into a compact, mode-locked SDL [43].

The availability and practicality of the pump source often defines whether an optically pumped laser is a feasible solution for a chosen application or not. Typically, the SDL is pumped with radiation with photon energy higher than that of the signal. Spectral requirements for the pump source are rather relaxed for these spacer/barrier pumped lasers, but the large quantum defect can be problematic for certain applications. Direct in-well pumping enables use of nearly equal pump and signal photon energies and offers an interesting way to convert pump radiation into signal [44]. Usually pump circulating optics are required in in-well pumped lasers, but due to the reduced quantum defect, the pumping can be highly efficient, with a reported optical-to-optical conversion efficiency in excess of 50% [23]. The laser can also be pumped electrically by direct injection of carriers into the quantum wells. Indeed, some of the very first vertical-external-cavity surface-emitting laser were electrically-pumped VCSELs in which the external mirror was used for spectral control [45] and suppression of higher order transversal-

Table 2.1: *State of the art cw optically-pumped semiconductor disk laser emitting at various wavelengths.*

Wavelength (nm)	Power (W)	Temp. (°C)	M^2	Year	Ref.	Comments
338	0.12	−10	N/A	2006	[36]	Frequency-doubled
391	N/A	27	N/A	2003	[18]	
460	1.9	0	N/A	2007	[1]	Frequency-doubled
488	15	N/A	N/A	2004	[11]	Frequency-doubled
535	7	20	N/A	2006	[2]	Frequency-doubled
575	8	N/A	N/A	2007	[3]	Frequency-doubled
612	2.68	7	N/A	2007	[S5]	Frequency-doubled
853	1.6	12	<1.1@1W	2007	[23]	In-well pumped
920	12	20	2	2007	[24]	
980	30	N/A	3	2004	[11]	
1000	8	0	<1.8	2003	[10]	
1055	4	15	<1.15	2006	[P1]	
1060	10	0	<1.7	2006	[37]	
1170	7	5	<1.46	2007	[25]	Tuning 1147–1197 nm
1240	1.46	8	N/A	2007	[S4]	
1320	0.6	5	<1.2	2004	[26]	
1541	0.78	−30	<1.2	2004	[29]	
2025	1	5	<1.45	2006	[P3]	
2360	2 3.2	15 −15	N/A	2007	[38]	In-well pumped

modes [46]. Electrically pumped devices have reached the 0.5-W power level in continuous wave single-transversal-mode operation [47] and are obviously independent of availability of pump diodes. However, difficulties in current spreading, optical absorbtion in doped semiconductor material and intensive processing requirements make these devices less attractive for research purposes, where quick processing and feedback on laser properties give the competitive edge.

2.3 View of the market and future art

The current market for commercial cw SDLs relies mainly on replacement of low-power (<0.5 W) ion lasers at 460 nm and 488 nm, used in various scientific, medical and industrial applications. In the future, the breakthrough market for SDLs and EP-VECSELs is presumably laser TVs and laser projection systems used in homes, offices and in portable electronics. So far the development of this market has been technologically hindered by the lack of green laser diodes. Frequency-doubled semiconductor micro-chip lasers are potential candidates to fill this gap. Eventually, the success of OP-SDLs in the market will depend on the component cost, wall plug efficiency, footprint and practicality of the pumping scheme. Undoubtedly a lot of development effort will be directed towards perfecting an optical pumping scheme that is compact and can be produced industrially at low cost.

In the author's view the medical and scientific market will expand to new wavelengths from 460 nm and 488 nm. The rapid development of blue GaN multi-mode diodes suggests that red SDLs could be pumped with diode lasers in the near future. Such progress would greatly promote commercial deployment of frequency-doubled SDLs emitting in the UV. The amber-orange-red spectral window is also commercially very interesting. As demonstrated in this thesis, GaInNAs/GaAs gain material offers a convenient way to access these wavelengths, but undoubtedly the technological boundaries of InGaAs/GaAs technology will be pursued in this quest in the future as well.

It is likely that the emission wavelength of GaSb-based SDLs is going to be pushed further towards and into the mid-infrared region, in part for purely scientific reasons, but also because of commercial motivation.

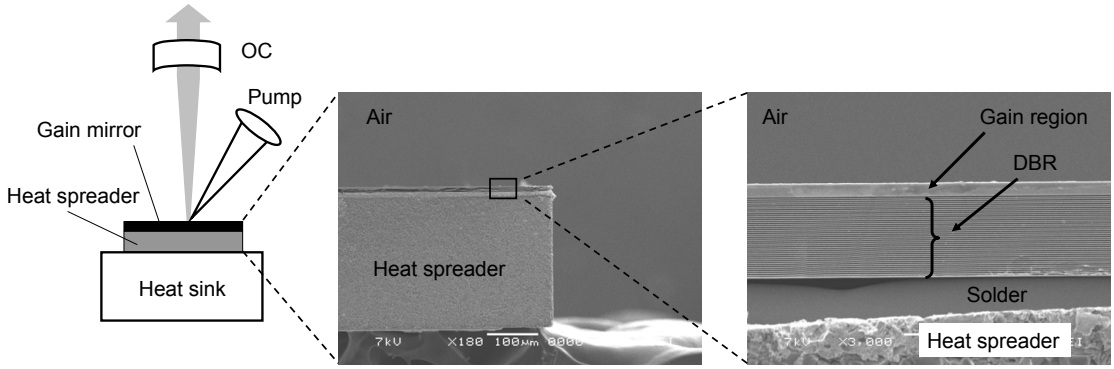

Figure 2.1: *Semiconductor disk laser: Simple linear cavity setup and SEM micrographs showing the gain mirror. OC = Output coupler, DBR = Distributed Bragg reflector.*

To the author's knowledge, the very first lasing *quantum dot* (QD) SDLs were demonstrated at the ORC by Jussi Rautiainen during the time of writing [48]. From a fundamental point of view it is interesting to see if QD-based disk lasers can provide additional benefits for spectral coverage, wavelength tuning and mode-locking.

2.4 Device structure

A semiconductor disk laser consists of a *gain mirror*, one or more external laser mirrors, and optical pumping of the gain, as presented schematically in Figure 2.1. The gain mirror is composed of a high reflective (HR) mirror and a *gain region*, sometimes also called the active region. Effectively, one of the laser mirrors is integrated with the gain element and this entity is called the gain mirror. The HR mirror is commonly formed of a stack of thin semiconductor layers constituting a *distributed Bragg reflector* (DBR), also called a Bragg stack. This allows the reflector and the gain region to be grown on a semiconductor substrate in a single epitaxial growth step. It should be noted, however, that the gain region and the reflector can be fabricated separately, as shown in [4], where a multi-layer semiconductor gain region was used with a metallic reflector. Dielectric materials, such as SiO_2 and HfO_2, may also be used to fabricate the DBR [18]. Dielectric materials can provide high index contrast, but they usually exhibit low thermal conduc-

tivity, which limits their use in high power applications. Metallic reflectors are usually avoided because of high losses. In certain cases a hybrid reflector combining a high contrast dielectric-semiconductor DBR and a metallic mirror [28] can offer sufficient reflectivity and heat transfer characteristics.

Several requirements should be met by the gain mirror. First of all, the materials in place must be transparent to the signal, yet the pump radiation must be absorbed efficiently. In contrast to edge-emitting diodes, laser action takes place in the direction normal to the semiconductor surface, resulting in a short interaction length of light in the gain medium. The typical thickness of the gain region is on the order of 1 μm, which is 2–3 orders of magnitude smaller than the interaction length in edge-emitting diode lasers. Consequently, single-pass gain is low and laser operation requires high quality gain material and careful control of cavity losses. In addition to the other requirements the thermal resistance of the layer structure should be low. The DBR, gain region, and thermal management are discussed in the following sections.

2.4.1 Distributed Bragg reflector

The distributed Bragg reflector is essentially a one-dimensional photonic bandgap structure, that reflects radiation at its forbidden bandgap or stopband. The design aims for high reflectivity in a spectral range defined by the application. Figure 2.2 presents a typical DBR reflectivity spectrum with a limited stopband of high reflectivity and multiple side peaks. The Bragg reflector is produced on a substrate of refractive index n_S, by stacking transparent thin-films of altering high n_H and low n_L refractive index, with each film having a quarter-wave optical thickness

$$d = \frac{\lambda_B}{4n(\lambda_B)}, \tag{2.1}$$

where λ_B is the *Bragg wavelength*, i.e. the target wavelength of maximum reflectivity and $n(\lambda_B)$ is the refractive index of the layer in question at the target wavelength.

Operation of the Bragg mirror is based on constructive interference of waves Fresnel-reflected from the layer boundaries. Light reflected within the low-index layers will experience a 180° phase shift, while that reflected within the high-index layers will not suffer any phase change on reflection. Consequently, the various components of the incident

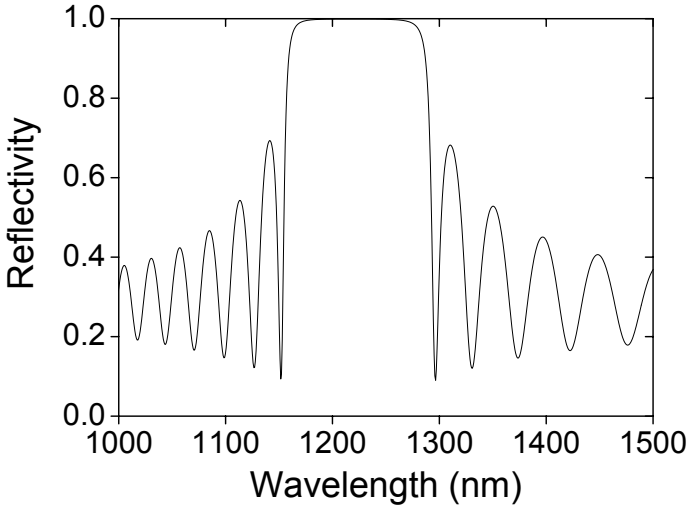

Figure 2.2: *Calculated reflectivity spectrum of a distributed Bragg reflector consisting of 30-pairs of GaAs/AlAs layers on GaAs substrate, designed for* $\lambda_B = 1220$ *nm wavelength.*

light produced by reflection at successive boundaries throughout the DBR assembly will reappear at the front surface all in phase, so that they will recombine constructively [49]. Reflectivity of a Bragg stack at λ_B is given [50] by

$$R_{2N}(\lambda_B) = \left(\frac{1 - (n_S/n_i)(n_H/n_L)^{2N}}{1 + (n_S/n_i)(n_H/n_L)^{2N}} \right)^2 \tag{2.2}$$

for a structure with an even number $(2N)$ of layers and by

$$R_{2N+1}(\lambda_B) = \left(\frac{1 - (n_H/n_i)(n_H/n_S)(n_H/n_L)^{2N}}{1 + (n_H/n_i)(n_H/n_S)(n_H/n_L)^{2N}} \right)^2 \tag{2.3}$$

for a structure with an odd number $(2N+1)$ of layers. In equations (2.2) and (2.3) N is the number of layer pairs and n_i is the refractive index of the surrounding medium, typically air. In order to provide the highest reflectivity, the DBR should begin with the layer of highest index contrast to the substrate and it should end with the layer of highest index contrast to the surrounding medium. Therefore, the substrate, DBR materials and the surrounding medium will determine whether the stack should consist of an even or odd number of layers.

Table 2.2: *Selected Bragg stack materials and structures with their optical properties. The substrate consists of the underlined material.* [51–54]

DBR materials	n_H/n_L	Δn	Number of layers	λ_B (nm)	$R(\lambda_B)$ (%)	$\Delta\lambda_{99\%}$ (nm)
GaAs/AlAs	3.49/2.99	0.50	60	1060	>99.9	99
GaSb/AlAsSb	3.89/3.22	0.67	36	2020	>99.8	203
InP/AlGaInAs	3.17/3.51	0.34	81	1550	>99.9	91
InP/InGaAsP	3.17/3.44	0.27	81	1550	>99.8	64
Au+Si/Al_2O_3	3.48/1.60	1.89	1+6	1550	>99.9	1036

It is evident from equations (2.2) and (2.3) that the reflectivity increases with increasing index contrast ($\Delta n = n_H - n_L$) and N. Reflectivity in excess of 99.9998% can be obtained using a large number of high contrast layers and careful fabrication procedures [55]. Ultimately, the DBR reflectivity is limited by the material absorbtion, scattering and stacking adhesion. The stopband width depends only on the index contrast, and is commonly given by

$$\Delta\lambda < 4\frac{\lambda_B}{\pi}\arcsin\left(\frac{n_H - n_L}{n_H + n_L}\right). \tag{2.4}$$

In SDLs the requirement of a low-loss cavity typically limits the usable bandwidth to $\Delta\lambda_{99\%}$, where the reflectivity $R \geq 99\%$. The reflection spectrum can be calculated conveniently using transfer matrix formalism [56], implemented in a number of commercial and free simulation softwares.

Ideally, the DBR should provide 100% reflectivity in a wide spectral range, yet it should have low thermal impedance and be lattice-matched to the substrate material. Table 2.2 presents an overview of common DBR materials and structures with their optical properties at applicable operation wavelengths. As one can observe from the table, GaAs and GaSb-based systems offer high index contrast DBR materials, namely GaAs/AlAs and GaSb/AlAsSb. The development of InP-based disk lasers, on the other hand, has been hindered by the lack of lattice matched high index contrast DBR ma-

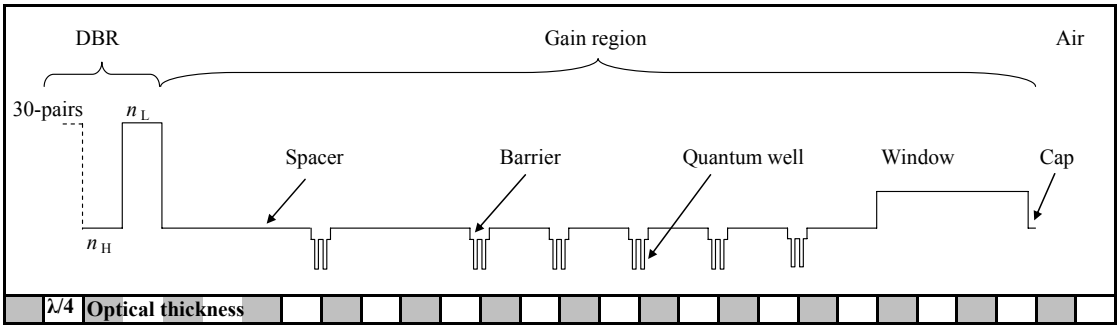

Figure 2.3: *Energy band profile of an SDL gain mirror with 6×2 quantum wells.*

terials. Attempts to circumvent this problem have led to the use of non-semiconductor based reflectors on InP and development of GaAs-based lasers operating at wavelengths traditionally covered by InP. A detailed discussion of the issue is provided in chapter 4.

2.4.2 The gain region

A typical SDL gain region consists of a *multiple quantum well* (MQW) structure grown epitaxially on the DBR, as illustrated schematically in Figure 2.3. The presented gain structure includes six groups of two quantum wells surrounded by barrier layers and intermediate spacer layers. The pump radiation, absorbed by the QWs, barriers and spacers, generates free carriers that are trapped in the quantum wells, generating photons by radiative recombination of electron-hole pairs. The gain mirror is completed with a large bandgap window layer that prevents carrier migration to the sample surface and consequent loss due to surface recombination. A thin (∼5–20 nm) cap layer can be grown on the window layer to protect it from oxidation, if this is anticipated.

The gain region forms a Fabry–Pérot micro-cavity between the DBR and the air boundary with ∼30% Fresnel-reflection. For gain enhancement, the quantum wells are usually positioned at the antinodes of the standing field localized in the micro-cavity [57]. Such design is commonly known as the *resonant periodic gain* (RPG). The resonant effect increases the effective light-matter interaction length by re-circulating signal in the micro-cavity. Therefore, the laser becomes more tolerant to cavity losses. The resonant effect can be enhanced by growing a top DBR on the gain region with

reflectivity of many tens of percent [58]. The resonant cavity provides gain enhancement only in a limited spectral range near the resonant wavelength, where the dispersive properties of the structure are also strongly modified. Consequently, tunable and mode-locked SDL structures are often purposely designed to be anti-resonant, by adjusting the window layer thickness and thus the *free spectral range* (FSR) of the cavity accordingly.

The intensity and spectrum of spontaneous emission are also affected by the resonant effect, making it difficult to resolve the true *photoluminescence* (PL) of the quantum wells from the cavity enhanced spontaneous emission, or "PL", emitted vertically by the gain mirror under illumination of pump light. This hinders the wafer characterization for two reasons. Firstly, the quantum well quality can not be determined from the "PL" intensity, neither can it be compared with other samples. Secondly, the spectral offset of the cavity resonance and PL-maximum can not be determined from the "PL".

A number of techniques have been developed to address the problem: the PL can be measured from the edge of the sample, in the direction parallel to the semiconductor plane [59], it can be recorded from a PL sample grown prior to the SDL structure, or the DBR can be removed from the SDL by *reactive ion etching* (RIE) to eliminate the cavity effect. While the first-mentioned method requires a sophisticated measurement setup, the last one involves an extensive amount of processing. Separate PL samples with quantum wells identical to those of the SDL structure provide a quick and simple way to estimate the PL properties. This approach was used extensively in this work. It should be mentioned, however, that this method is sensitive to changes in growth parameters, such as material fluxes, between successive growths and can, therefore, yield a certain inaccuracy.

The number and distribution of the quantum wells is a matter of optimization for each laser. We have obtained watt-level output using a gain structure with only 2 QWs, but usually $\sim$10–20 QWs produce the best balance between power, threshold and slope efficiency. The quantum wells or quantum well groups can be equally spaced (at the antinode positions) in the micro-cavity, but often the quantum well distribution is nonuniform and follows the density of carriers determined by the nearly exponential decay of the pump intensity in the structure. This feature is illustrated in Figure 2.3, where the last group of quantum wells is spaced an extra $\lambda/2$-distance away from the previous QW

group to compensate for the reduced carrier density. High bandgap carrier blocking layers may also be included in the gain region to separate independent gain sections from each other [57, 60] and to provide more uniform carrier distribution among different quantum wells or well groups. Use of carrier blocking layers is particularly important in the dual-wavelength SDLs as discussed in [S8].

The choice of barrier/spacer materials and structures also plays an important role in the design of the gain region [61]. Thus, significant improvements can be achieved with proper barrier/spacer optimization, particularly in devices with shallow quantum wells [60]. The function of the barriers is to promote efficient transfer of carriers from the spacers into the wells. The barriers and spacers are often also used as strain compensators for lattice misfit of the quantum well and the host material [9, 62]. Although all laser structures described in this thesis utilize multiple quantum wells, it should be noted that the active region may also be formed of multiple layers of quantum dots [48], or bulk material [5, 8].

2.4.3 Optical pumping

The optical pumping used in this work benefits from simple device processing and allows for multi-watt output powers. It avoids the use of absorbing doped materials and technological challenges characteristic of EP-VECSELs. In the spacer pumped design strong pump absorbtion is achieved without pump re-circulating optics and the absorbtion is practically independent of the number of quantum wells. Spectral requirements for the pump are relaxed, although at the cost of typical $\sim$15–35% loss due to the quantum defect.

2.5 Thermal issues

Thermal roll-over and thermal lensing are the dominant factors that limit the performance of an SDL. Heating of the gain structure originates from pump energy, which in addition to photon emission, also creates phonon emission due to non-radiative recombination and the quantum defect.

A number of semiconductor parameters, such as the band gap, gain spectrum, carrier confinement and distribution of electronic states depend on the temperature. Heating reduces the peak gain of an individual quantum well and causes a spectral shift. The rate of non-radiative processes, such as Auger recombination and defect induced non-radiative recombination, increases at elevated temperatures. The magnitude and significance of different temperature dependent processes depend on a variety of factors, such as the material composition, crystal quality and growth conditions [63, 64]. Importantly, these mechanisms can give rise to a self-supporting (positive) feedback loop that forces the laser output to "roll-over", when a threshold of pump power is exceeded. In the particular case of vertical-cavity lasers, heating also affects the spectral detuning of the micro-cavity resonance and the gain maximum.

Due to thermal expansion and a temperature dependent refractive index the physical and optical length of the semiconductor micro-cavity changes as a function of temperature, causing a spectral shift to the Fabry–Pérot resonance. The magnitude of this shift is $\sim$0.2 nm/K for GaAs at 1 μm wavelength, while the gain spectrum of InGaAs quantum wells shifts at a rate of about 0.4 nm/K. Obviously, a temperature change from the optimal point results in spectral walk-off and mismatch of the FP resonance and the peak gain, thus reducing the overall gain. The FP resonance and the gain peak are commonly pre-offset by design at room temperature and reach the matching point at the operation temperature. Still, the optimal device design aims to minimize the temperature rise and maintain optimal conditions over the whole range of available pump power.

Thermal lensing may not directly limit the output power of the laser, but it can significantly degrade the beam quality. Thermal lensing means formation of an effective lens in a solid state medium under a temperature gradient. A thermal lens can be related to a physical lens being formed by surface curvature under non-uniform thermal expansion. More important to SDLs, the temperature gradient induces an index gradient and leads to the formation of a GRIN lens in the material in question. Thermal lensing usually disturbs the original cavity design, but can also be exploited, particularly in quasi-stable micro-chip lasers with plane–plane cavity, where it is used to stabilize the cavity and define the cavity mode [65].

In an SDL the thermal lens is formed in the gain mirror and in the intracavity heat

spreader element, if such is implemented in the design. Thermal lensing gradually changes the cavity geometry as a function of pump power. Usually the cavity is designed to tolerate such disturbances without loss of stability, but the shape of the fundamental laser mode can be modified, leading to mismatch of the laser mode and the pump spot. This mismatch allows for the emergence of higher order transversal cavity modes that utilize the untapped gain outside the fundamental mode area. Consequently the output beam quality is reduced.

To avoid the detrimental thermal effects, the laser design must accept a large heat load (intense pumping) without significant temperature rise. In simple terms, the component should have high thermal admittance and it should operate with high wall-plug efficiency. The conversion efficiency is largely determined by the quantum defect, semiconductor crystal quality and gain mirror/cavity design. Thermal admittance, on the other hand, can be improved to a large extent by suitable heat sinking and processing methods.

A number of theoretical and experimental studies [66–69] have been published on thermal issues and heat flow in the gain mirror structures, where the heat generation occurs in a point source under intense optical pumping. The diameter of the pump spot is typically much larger (tens or hundreds of microns in diameter) than the thickness of the gain mirror (a few microns), making the heat flow in the thin-film structure essentially one dimensional, perpendicular to the semiconductor plane. The key point for effective heat dissipation is distribution of thermal energy in the lateral dimension, i.e. heat spreading from the point source. An enlarged dissipation area allows for enhanced heat extraction and reduces the thermal resistance of the component. The processing steps and methods for obtaining reduced thermal resistance are discussed in the following section.

2.6 Device processing

Two different techniques are widely used in SDLs to dissipate the heat load - the flip-chip bonded thin-device approach introduced by M. Kuznetsov [9] and the intracavity heat spreader approach [70]. The schematics of lasers based on these techniques are

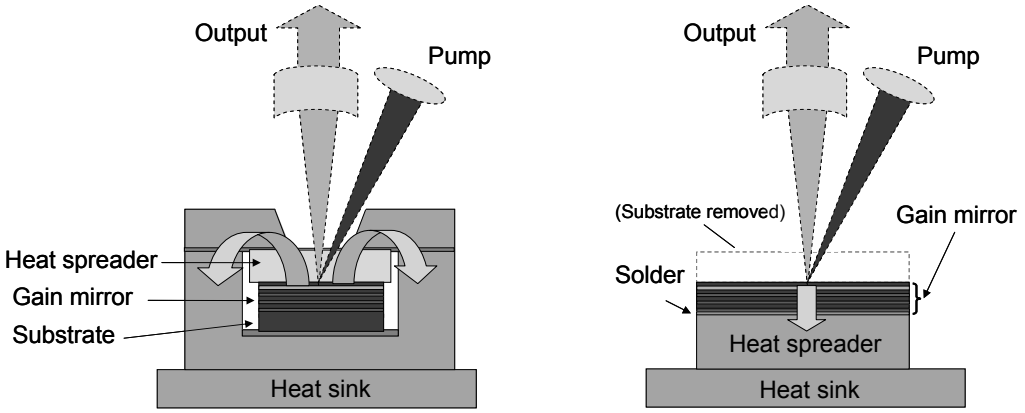

Figure 2.4: Left: *Semiconductor disk laser utilizing a transparent intracavity heat spreader.* Right: *Flip-chip bonded device with removed semiconductor substrate. Direction of the heat flow is presented with the arrows.*

presented in Figure 2.4 showing the path of heat transportation in each system. During this work, we have studied both heat management techniques and developed suitable processing procedures. However, only devices based on the intracavity heat spreader approach are reported in the related publications of this thesis. In terms of power and beam quality we have not observed large differences in the two approaches, at least not for GaAs-based devices. The pros and cons of each approach become more apparent and pronounced when one compares the cost, time of processing, spectral characteristics and mode-locked operation. For InP-based lasers the intracavity heat spreader approach could present clear advantages, because the DBR with high thermal resistance is excluded from the path of heat flow. To the author's knowledge, at the time of writing, no extensive comparative study has been published on the long term stability and performance of these techniques.

2.6.1 Flip-chip bonded device

For flip-chip mounted device, first an etch stop layer is grown onto a semiconductor substrate, followed by the gain section and finally by the DBR. After metallization and mechanical thinning a chip is scribed off the wafer and soldered, DBR down, to a heat

spreader of high thermal conductance, such as diamond, copper or their composite, for instance. The remaining semiconductor substrate ($\sim$100 μm) is removed from the bonded chip by means of selective etching. The detailed structure of a flip-chip bonded thin-device is evident from Figure 2.1 in which scanning electron microscope (SEM) pictures of such a component are presented.

GaInP material is commonly used as an etch-stop on GaAs. It is not prone to oxidation, works well as a window layer, and allows for removal of the GaAs substrate with a high degree of selectivity using NH_4OH:H_2O_2 (1:30) etchant. For improved surface quality one may also use multiple etch-stop layers as described in [71]. After thin-device processing the substrate with high thermal resistance is completely removed and does not obstruct heat flow, nor is it located in the laser cavity, which results in increased optical absorbtion. Effectively the epitaxial layers are transferred from their original substrate onto a high thermal conductance host, for which reason the procedure is sometimes referred to the *epitaxial lift-off* (ELO) process.

High quality bonding is crucial to the success of the process. For low power and short term applications one can use soft solders such as indium, which relieve mechanical stress between the sample and the heat spreader and are easy to use. Temporally and thermally more stable hard solders, such as AuSn, are usually used in demanding applications. Unlike indium, AuSn can also resist HCl-based etchants used for removal of InP substrates. Hard solders don't alleviate stress and therefore the *coefficient of thermal expansion* (CTE) must be rather similar for the sample and the heat spreader. Commercially available diamond-copper composites are particularly well suited for this purpose and they can be ordered with the solder pre-deposited on the surfaces. This is a clear advantage since a few micrometers thick solder preforms are difficult to handle manually. We have carried out the AuSn bonding process in a reflow-vacuum chamber, where N_2 and forming gas can be used to prevent oxidation or actively remove oxides from the sample and the solder. Use of vacuum at high temperatures, where the solder is in molten form, removes air bubbles from the solder and, therefore, reduces the number of voids.

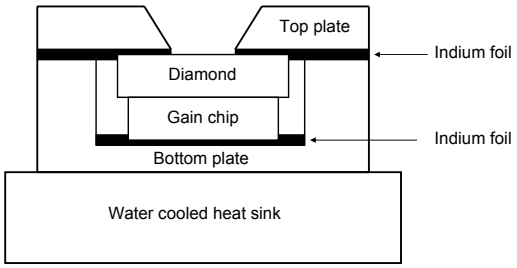

Figure 2.5: *Schematic presentation of the mounted gain mirror and intracavity diamond heat spreader.*

2.6.2 Intracavity heat spreader approach

The other commonly used heat management technique exploits an intracavity heat spreader and takes advantage of transparent materials with high thermal conductance, such as diamond, SiC and sapphire. In terms of device processing, this approach is less demanding than flip-chip bonding and processing. The intracavity heat spreader approach allows for direct heat extraction from the gain region and is well suited for structures with a DBR of high thermal resistance. An intrinsic feature of this technology is that the heat spreader adds a Fabry–Pérot etalon to the cavity and periodically modulates the output spectrum, which is often not desired. On the other hand, a thin heat spreader with large FSR can also force narrow band or single-longitudinal mode operation [34].

In this design the gain mirror is grown in the ”normal” order; the DBR is grown on the substrate first and is followed by the gain region. A small chip is then scribed off the as-grown wafer and brought into physical contact with the heat spreader by the capillary action of water, methanol or other suitable liquid or simply by pressing it mechanically. We have used diamond heat spreaders, for their superior thermal conductance ($\sim$2000 W/m·K). However, the cost of natural diamonds scales more or less exponentially with their size, and for that reason we limited the size of our gain chips to 2.5×2.5 mm^2 and the diamond size to $3 \times 3 \times 0.3$ mm^3. More cost-effective synthetic single-crystal diamonds used in this work were circular disks with 4 mm diameter and 0.5 mm thickness.

For efficient heat conduction the components were mounted between two copper plates, as presented in Figure 2.5. A square shaped recessed area was machined to the

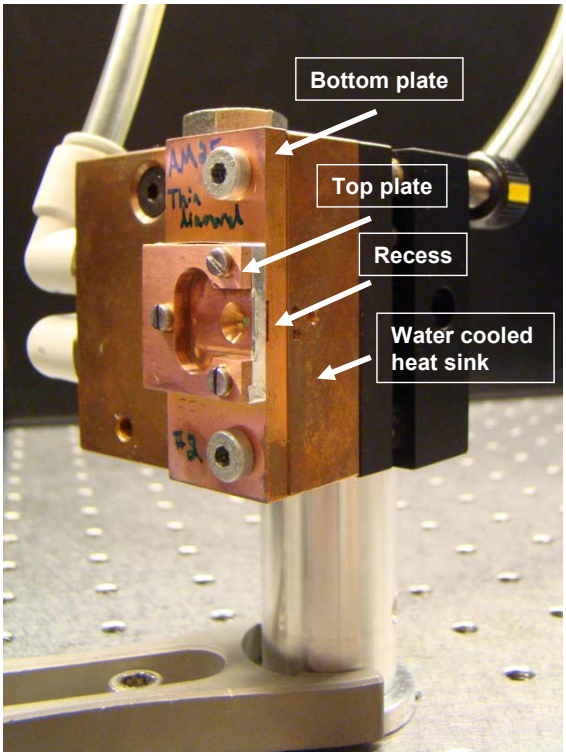

Figure 2.6: *Photograph showing the sample mounting.*

bottom plate, where the gain mirror was fitted on a sheet of indium foil. The top plate has a flat contact surface and a circular ($\varnothing \sim 1.5$ mm) aperture in it to allow free travel of pump and signal radiation. The edges of the opening were machined at a 45° angle to the surface normal to allow pumping at an angle. A wide machining angle also prevents the screening effect if an *antireflective* (AR) coating is deposited at a later time onto the diamond surface through the aperture.

A sheet of indium foil was contacted to the lower surface of the top plate, before it was tightened by screws to the bottom plate. The mount was attached to a water cooled copper heat sink on a mirror mount with 2-axis tilt, as shown in Figure 2.6. Heat from the sample is first conducted through the heat spreader to the top plate, further on to the bottom plate and finally to the heat sink. The design does not allow for large tolerances in the depth of the recessed area; while too deep a recess prevents the contact between the heat spreader and the top plate, too shallow a recess forces the heat spreader to protrude

Table 2.3: *Typical thicknesses of the gain chip, heat spreader, and indium foil.*

$d_{gainchip}$	$d_{heatspreader}$	$d_{indiumfoil}$	d_{recess}
380 μm	310 μm	50 μm	715 μm

from the bottom plate and breaks the thermal contact between the top and bottom plates. The only tolerance available is the depth to which the bonded sample indents into the indium foils. Therefore, the depth of the recessed area is a critical parameter to the functioning of the device and is given by $d_{recess} = d_{gainchip} + d_{heatspreader} + 0.5 \cdot d_{indiumfoil}$, with typical values listed in Table 2.3. This arrangement allows for ± 10 μm machining tolerance for the recessed area, without detriment to the functioning of the component. On average the total indentation of the sample into the indium is about 25 μm, which ensures firm mechanical contact between sample and the mount. Since the diamond and the semiconductor wafer thicknesses can vary by tens of microns from batch to batch, it is usually necessary to fabricate a specific mount for each and every component with a fixed recessed area depth.

It should be noted that a flexible "one-size-fits-all" mounting system can be arranged by integrating the heat sink and the top plate and then pressing the component onto the top plate with a clamp, as presented in [72]. Such a system allows rapid change of test samples and supports any sample/diamond thickness without modifications to the mount. This arrangement has clear advantages when fast feedback is required from a large number of samples. On the down side, this approach does not preserve the components in a fixed mount for use at a later time. Therefore, it is not usually cost effective to deposit AR coatings on these components.

2.6.3 Capillary bonding

Capillary bonding is a method in which two flat and smooth surfaces are pulled into close contact by liquid surface tension and bonded together by intermolecular surface forces. The method does not require use of external force, thermal treatment or ad-

hesives, which makes it extremely simple and user friendly. Capillary bonding has been used successfully for attaching epitaxial lift-off layers onto arbitrary substrates, as demonstrated in [73], where the method was referred to "Van der Waals" bonding, because of the presumed role of the interfacial forces. In 2000 Z. L. Liau published a report on capillary bonding of semiconductor wafers [74] and later on the method was adopted for the fabrication SDLs [70].

Unlike ELO layers, semiconductor wafers and diamond heat spreaders can not adapt flexibly to surface undulations and therefore the requirements for surface flatness, smoothness and cleanliness are stringent. "Epiready" semiconductor wafers are naturally suited for the process as such, but large and numerous growth induced defects, rough scribing edges and any dirt or dust particles can prevent proper bonding. The nitrogen-free type IIa natural diamonds used in this work had a surface roughness (Ra) below 15 nm and a defined surface flatness of < 3 interference fringes in reflection at a wavelength of 632.8 nm. For single-crystal synthetic diamonds the same parameters were: roughness < 5 nm (Ra) and flatness < 0.5 fringes. Prior to bonding, the sample and the diamond were inspected with a prism microscope and thoroughly cleaned with pure (99.5%) ethyl alcohol and re-checked with the microscope. If required, one may also consider ultrasound cleaning in acetone and methanol for enhanced removal of impurities. The gain mirror was wetted with de-ionized water and the heat spreader was placed on top of it. Light pressure was used to force out excess water and leave only a micrometers thin film of liquid in between. As the water film slowly evaporates from the sides, the diamond and the gain mirror are pulled into closer contact. The separation can be in-situ monitored from thin-film interference fringes (Newton's rings) representing areas of equal thickness. Film thickness at various interference maxima (m) is $d = (m + \frac{1}{2})\frac{\lambda}{2}$, where $(m = 0, 1, 2, \ldots)$ [75]. Therefore, the difference in film thickness for adjacent maxima is $\lambda/2$. Use of force is not required in the process, but subtle lateral displacement of the diamond may promote quicker bonding. Contact is usually reached in a circular area at the center within 5–15 minutes, after which the surrounding Newton's rings start to disappear at an accelerated rate as the bonding proceeds. The sample may be bonded over the whole area or only partially, depending on the quality of the heat spreader and the gain mirror. A significant mechanical force is required to disassemble a well-bonded

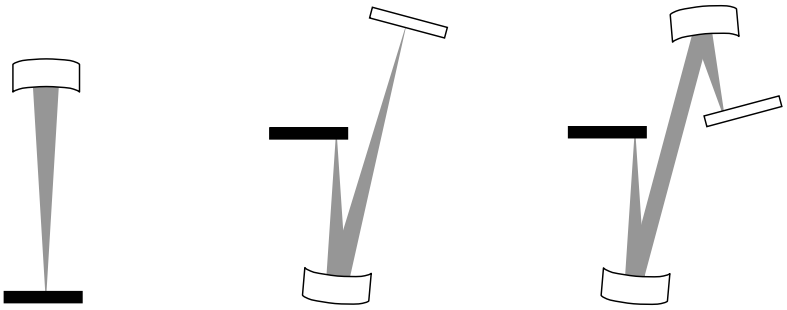

(a) I-cavity (b) V-cavity (c) Z-cavity

Figure 2.7: *Schematics of common SDL cavity configurations. The gain mirror is represented by the black bar, while the white components represent passive mirrors.*

component. Usually the edges of the sample become pulverized before the bonding gives in under mechanical force. However, the heat spreader can be conveniently dismounted from the sample by placing the component in water (or another suitable liquid). Use of two high quality wafers for the bonding experiment can result in solid bonding that does not break in water, but we have never observed this with diamond bonding. A clear advantage of diamond heat spreaders is that they are not easily scratched and can be re-used multiple times.

2.7 Resonator design

The geometry and properties of the laser resonator, or the cavity, are an important part of the laser design. Firstly, the resonator should be stable, i.e. the beam must reproduce itself after each round-trip in the cavity. To suppress any higher order transversal-modes, the geometry should ensure that the size of the fundamental Gaussian mode closely matches the pump spot size on the gain mirror. The pump spot and output coupling should be designed in regard to available pump power and gain. Some common variants of I-, V-, and Z-shaped resonators are presented in Figure 2.7.

Chapter 3

Diamond heat spreaders

3.1 Effect on laser performance

The choice of heat spreader material plays an important role, both in terms of device performance and cost. Synthetic single-crystal diamonds are commercially available in large sizes with excellent surface quality and can offer a significant cost reduction in comparison to natural diamonds. Within this work we compared natural type IIa and synthetic type IIIa diamond heat spreaders using a simple V-cavity configuration and 1055 nm gain material.

The gain elements used in the comparative study were taken from the same epiwafer. The layer structure, described in [P1], included a 30.5-pairs GaAs/AlAs DBR and 13 InGaAs QWs in a resonant periodic gain structure. The quantum wells were placed non-uniformly in the microcavity in 3 groups of 3 QWs and 2 groups of 2 QWs located at the antinodes of the standing wave. The QWs were positioned properly using GaAs spacer layers and thin AlGaAs carrier blocking layers between each group. The test samples included similar dual-layer TiO_2–SiO_2 AR coatings on the diamonds. Sample 1 utilized a capillary bonded, type IIa natural diamond, with thickness $d = 300$ μm. Sample 2 included a heat spreader platelet with the same specifications as sample 1, but it was mechanically clamped onto the gain mirror by the copper mount assembly, without prior capillary bonding. Sample 3 had a 500-μm thick capillary bonded single-crystal synthetic type IIIa diamond heat spreader.

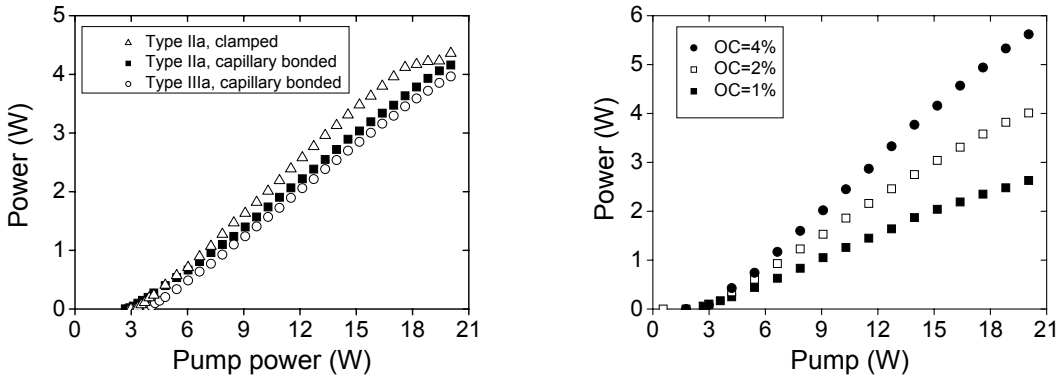

(a) (b)

Figure 3.1: *(a) Output power of the lasers with a 2% output coupler, given as a function of incident 808-nm pump power. (b) Output characteristics of the sample with capillary bonded type IIa diamond, using 1%, 2% and 4% output coupling (OC).*

The samples were characterized in the same laser setup at a 15 °C mount temperature and using a 2% output coupler. The geometry of the cavity was kept unchanged for each sample. The light output characteristics, presented in Figure 3.1(a), reveal surprisingly similar output characteristics for all three samples. Sample 3, with the artificial diamond, had a slightly higher threshold and smaller output power than the two other samples. This tendency was also observed in later studies. The capillary bonding process was not inherently superior to mechanical clamping in terms of device performance. However, firm bonding indicates good surface quality and close contact of the sample and the heat spreader platelet, thus promoting processing of uniform quality. For this reason capillary bonding was used later in this work as the main processing technique.

Further studies of the laser properties were carried out with the capillary bonded component. With a 4% transmissive output coupler we obtained 5.62 W of output power at an incident pump power of 20 W (Figure 3.1(b)), corresponding to 28% optical-to-optical conversion efficiency. It should be noted, however, that the beam quality factor M^2 reduces at the highest powers. When the laser was characterized with a 2% output coupler, single-transversal-mode operation could be maintained throughout the operation range, with $M^2_{x,y} \leq 1.15$ at maximum output power of 4 W. The laser spec-

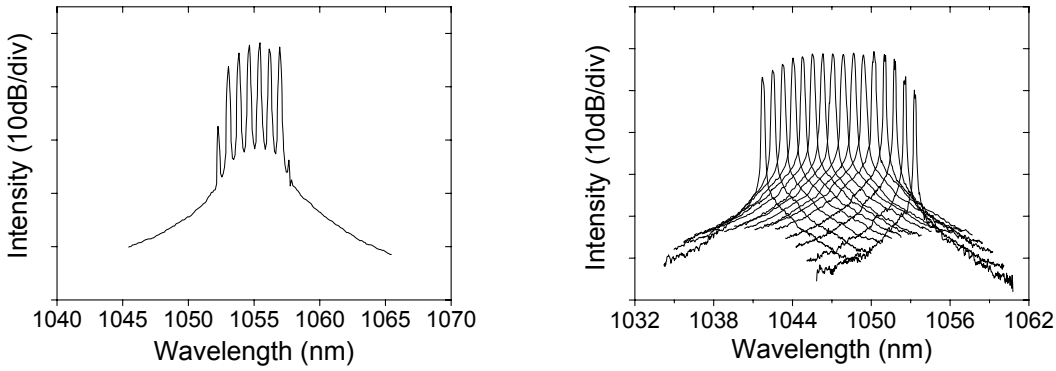

(a) (b)

Figure 3.2: *(a) Optical spectrum from a laser with 2% output coupler at 20 W of pump power. (b) Several narrow band spectra selected discretely with a birefringent tunable filter.*

trum, presented in Figure 3.2(a), had a comb-like shape with multiple peaks spaced by $\Delta\lambda \approx 0.77$ nm. The multi-peak spectrum originates from the Fabry–Pérot etalon that is formed inside the laser cavity by the diamond heat spreader. The spacing of the emission peaks correlates accurately with the free spectral range $\Delta\lambda_{\mathrm{FSR}} = \lambda^2/(2nd) = 0.775$ nm of the diamond, assuming $\lambda = 1.055$ μm, $d = 300$ μm and $n = 2.394$ [76]. The smooth shape and regular spacing of the emission peaks often indicates single-transversal-mode or nearly single-transversal-mode operation. By inserting a birefringent filter in the cavity at the Brewster angle, we could select the emission peaks one by one over a range of 11.6 nm, as illustrated in Figure 3.2(b). The tuning was discrete, with the step set by $\Delta\lambda_{\mathrm{FSR}}$. The etalon effect could not be completely avoided with the 2-layer AR coating. Antireflective coatings were applied throughout this work, since they increase the pump transmission and often also improve the beam quality significantly.

In conclusion, we obtained 4 W of 1055 nm radiation near room temperature with $M^2 \leq 1.15$ from the sample with capillary bonded natural diamond heat spreader, using 2% output coupling and 20 W of 808-nm pump power. The use of a synthetic diamond heat spreader provided nearly equal laser performance and offered significant cost reduction in comparison to the natural diamond platelets. Simple mechanical clamping of the heat spreader onto the sample resulted in equal or even improved laser performance

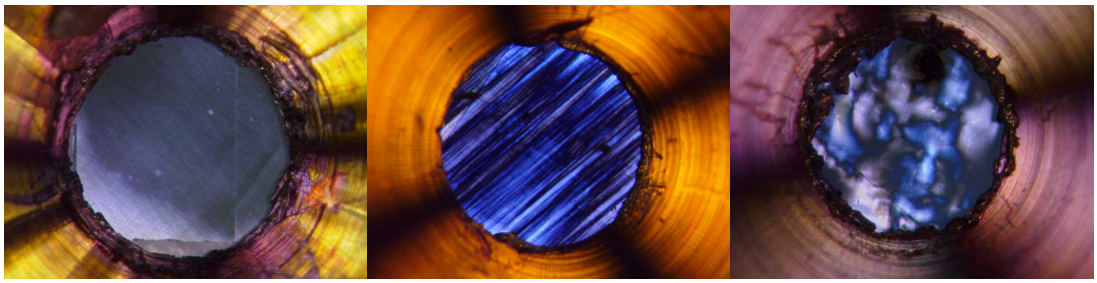

(a) Type IIa (b) Type IIa (c) Type IIIa

Figure 3.3: *Polarization micrographs of two type IIa natural diamonds (a) and (b), and a synthetic type IIIa diamond (c) used as heat spreading elements in disk lasers. All diamonds are bonded to a gain mirror chip, placed in a copper mount and viewed through a* $\varnothing \sim 1.5$ *mm aperture in the mount. The changes in color result from variations in the magnitude and orientation of birefringence of the material. Therefore, it is expected that the diamond shown in (a) has nearly isotropic crystalline structure, while the sample shown in (b) exhibits birefringent properties with uniform orientation and the sample shown in (c) has various areas with different orientation and magnitude of birefringence.*

in comparison to capillary bonding.

3.2 Birefringent properties

Although the use of synthetic and natural diamond heat spreaders resulted in very similar laser performance, there are still fundamental differences in their optical properties, which affect their use in lasers with polarization selective elements, as reported by Van Loon et al. [77]. The authors studied the birefringence of different natural and synthetic diamond heat spreaders and its effect on the laser performance in the presence of an intracavity Brewster plate. It was observed that the single-crystal synthetic diamonds have areas with non-uniform orientation of material birefringence. The natural diamonds used in the study presented either negligible birefringence or low birefringence with uniform orientation. It was verified both theoretically and experimentally that the retardation presented by the birefringent diamond plate could result in a significant loss in the presence of the Brewster plate. The loss could be avoided by proper angular orientation of the

natural diamond in respect to the Brewster plate, i.e. by rotating the diamond in such a way that the orientation of the birefringence coincided with the orientation of the laser's polarization defined by the Brewster plate. Due to the random nature of birefringence orientation in synthetic diamonds, a similar loss reduction is difficult to achieve. It is unlikely that synthetic diamonds are suitable for commercial disk lasers that use polarization selective elements in the cavity. On the other hand, the cost of natural diamonds prevents their use in low-cost lasers. Silicon carbides could provide a commercially and technically feasible alternative to diamonds. Yet again, the flip-chip approach intrinsically avoids all problems related to the birefringence, etalon formation and expensive heat spreaders.

The diamonds used in this work were inspected with a polarizing microscope (Figure 3.3), and they indicated similar properties to the ones characterized by Van Loon et al. All inspected natural diamonds presented nearly isotropic properties as shown in Figure 3.3(a), or birefringence with well determined orientation, Figure 3.3(b). Synthetic diamonds, on the other hand, had areas where the magnitude and direction of birefringence was different from the neighboring areas, Figure 3.3(c). Based on these observations and the results presented in [77], it was concluded that diamonds with isotropic crystal lattice should always be used with lasers that include polarization selective elements.

Chapter 4

Frequency-doubled GaInNAs disk laser emitting in the red

This chapter concerns the generation of 615 nm red emission using a frequency-doubled GaInNAs/GaAs-based disk laser operating near 1230 nm. Challenges related to generation of laser radiation at this wavelength, as well as the frequency-doubling scheme and obtained results are discussed.

4.1 Introduction

The spectral window of interest to this work is located between 580 nm and 630 nm and covers the colors amber-orange-red. Lasers in this spectral band are used in various medical, scientific and display applications. Unfortunately, it is difficult to produce the desired colors directly with conventional GaInP-AlGaInP/GaAs semiconductor lasers, due to lack of direct bandgap barrier materials that would provide good confinement of the photo-generated carriers in the quantum wells. Therefore, complicated dye-, ion-, and gas-lasers [78], as well as OPO and DPSSL systems [79,80] have been used instead. Frequency-doubled infrared disk lasers could replace existing laser systems in certain applications and provide substantial cost reduction: a concept that works well at 488 nm. The work presented in this chapter was mainly motivated by the need to produce high power red emission for RGB applications.

4.2 Accessing 1160–1260 nm spectral region

The targeted visible wavelengths can be produced by frequency-doubling infrared laser radiation at 1160–1260 nm. This spectral range is difficult to achieve with traditional InGaAs/GaAs technology due to significant lattice-mismatch and consequent build-up of strain in the semiconductor crystal lattice. This problem is even more pronounced for high power lasers such as the SDL.

One could resort to InP based gain materials at least in part, but it has been challenging to transfer InP technology from edge-emitting lasers to surface-emitters, mainly due to the lack of good DBR materials. A number of lattice-matched DBR compounds have been developed such as AlGaInAs/AlInAs [81,82], AlGaInAs/InP [83,84], GaInAsP/InP [85, 86], AlGaAsSb/AlAsSb [87, 88] and AlGaAsSb/InP [89].

Unfortunately, the above mentioned DBRs suffer from either low index contrast, low thermal conductivity, or high complexity of growth. High performance DBRs can be processed on an InP gain region after epitaxial growth, by metallic dry bonding [28], wafer fusing [90, 91] or by sputtering/e-beam evaporation. However, the most desirable way to fabricate surface-emitting laser structures is by monolithic growth of the DBR and the active region. To circumvent the problems of InP-based DBRs, various alternative approaches have been introduced based on GaAs technology operating at longer wavelengths than the typical InGaAs window near 1 μm:

- GaAsP strain compensation and a small number of InGaAs QWs on GaAs [92], VCSELs demonstrated at 1.3 μm [93].
- GaAsSb quantum wells on GaAs [94], VCSELs demonstrated at 1.3 μm [95].
- GaInNAs quantum wells on GaAs [96], VCSELs at 1.3 μm, edge-emitters at 1.5 μm [97].
- InAs-InGaAs quantum dots on GaAs, numerous demonstrations with VCSELs in the 1.3 μm telecom window [98, 99].
- GaInNAsSb quantum wells on GaAs [100], VCSELs at 1.5 μm and beyond [101].

While these advances in material development were driven forward by the needs of optical telecommunications at 1.3 μm and 1.5 μm, they have also had a significant impact

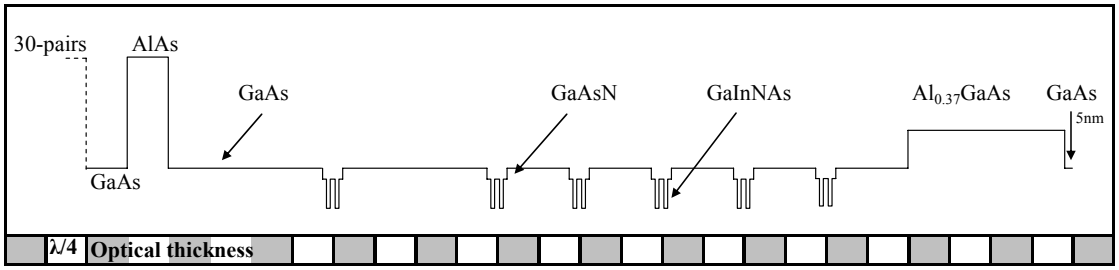

Figure 4.1: *Dilute nitride gain structure including 6×2 GaInNAs quantum wells of 7-nm thickness.*

on the development of semiconductor disk lasers; multi-watt SDLs based on strain-compensated InGaAs QWs have been reported at 1160 nm [3] and 1170 nm [25], of which the former was used for generating frequency-doubled yellow emission and the latter could be tuned upto 1197 nm with ∼25 mW power. Orange-red radiation from a 1220-nm SDL was reported by Gerster et al. [78] using GaAsSb/GaAs gain material and Hopkins et al. demonstrated 1.3 μm emission from a dilute nitride GaInNAs disk laser. Here we used GaInNAs/GaAs gain material and an intracavity frequency-doubling scheme to demonstrate high power 615 nm emission from a disk laser.

4.2.1 The gain structure

The GaInNAs gain mirror was grown on an n-type GaAs (100) substrate by molecular beam epitaxy, equipped with an RF-plasma source for incorporating nitrogen into the crystal lattice. First, a 30-pair GaAs/AlAs Bragg stack was grown on the substrate and it was followed by a 12 GaInNAs QW resonant periodic gain structure, presented in Figure 4.1. The 7-nm thick quantum wells were paired in six groups and distributed non-uniformly in the 5.5-λ long cavity. Compressive strain of the QWs was alleviated by tensile-strained GaAsN layers surrounding each QW. The active region was finished with an $Al_{0.37}Ga_{0.63}As$ window layer and a thin GaAs cap. A detailed description of the epitaxial growth of the sample is given in [102].

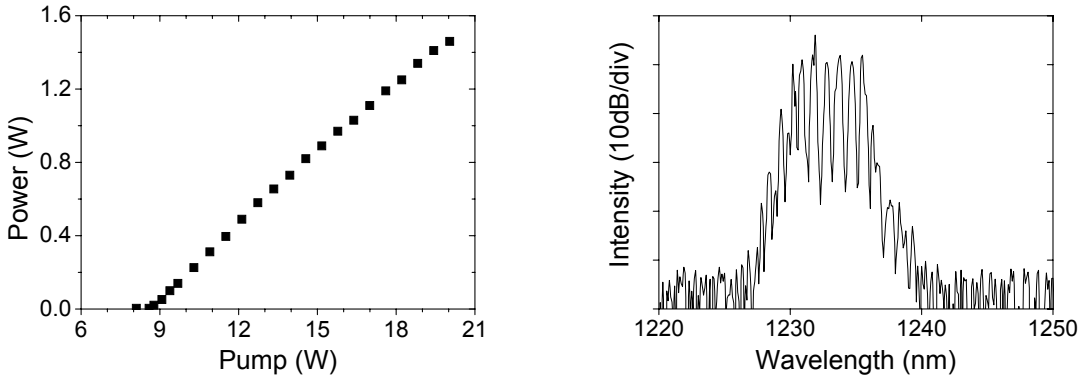

Figure 4.2: *(a) The output power of the 1230 nm disk laser given as a function of the incident 808-nm pump power. (b) Output spectrum at 20 W of pump power, $T = 8\,^{\circ}C$.*

4.2.2 Laser performance at 1230 nm

Prior to the SHG experiment, the laser performance was studied at the fundamental frequency using a V-shaped cavity and 1% output coupling [S4]. The gain chip included a 300-μm thick intracavity diamond heat spreader with an AR coating. The gain mirror was pumped with 20 W of 808-nm radiation, focused to a $\varnothing \sim 180$ μm spot. The light output characteristics, shown in Figure 4.2(a), were recorded with a pyroelectric power meter at mount temperature of 8 °C and reveal 1.46-W maximum continuous wave power. At $T = 35$ °C we obtained about 1 W output.

Interestingly, it was observed that the threshold decreased when the mount temperature was increased. This phenomenon was interpreted as being due to a shift of the gain spectrum towards the center of the DBR stopband. The rate of the temperature dependent gain shift, measured from a PL sample, was about 0.44 nm/K, which corresponds to the observed 12-nm shift of the laser spectrum with an increase in temperature from 8 to 35 °C. The laser spectrum at 1230 nm was measured using multi-mode optical fiber coupling and an optical spectrum analyzer (Ando AQ-6315A). The laser spectrum is presented in Figure 4.2(b).

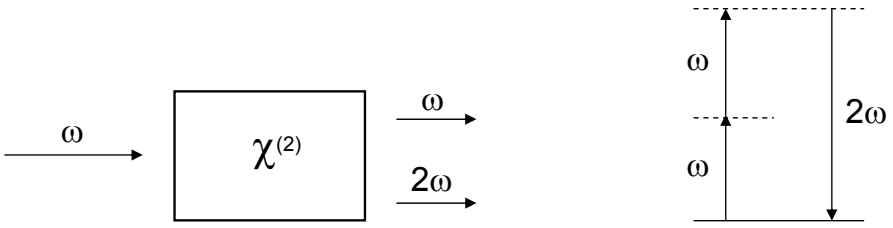

Figure 4.3: Left*: Schematic illustraton of second-harmonic generation in* $\chi^{(2)}$ *material.* Right*: Energy level diagram presenting generation of the second-harmonic frequency* 2ω*. The solid line represents the atomic ground state, whereas the dashed lines represent so called virtual levels.*

4.3 Second-harmonic generation

Nonlinear frequency conversion is a key technology which allows access to wavelengths for which lasers are not available or for which they come in an impractical form. Coherent radiation in UV, visible and mid-infrared regions is commonly produced using frequency-converted near-infrared lasers. Frequency-doubling, or *second-harmonic generation* (SHG), is a phenomenon where a wave with frequency ω generates a second-harmonic wave at optical frequency 2ω in suitable nonlinear material, as schematically presented in Figure 4.3.

4.3.1 Theoretical considerations

Formation of the second-harmonic wave can be understood by considering an electromagnetic wave, with electric field

$$\tilde{E}(t) = Ee^{-i\omega t} + E^* e^{i\omega t} \tag{4.1}$$

travelling in an anisotropic optical crystal whose second-order susceptibility $\chi^{(2)}$is nonzero. The polarization in the material in the presence of the field is then given by

$$\tilde{P}(t) = \chi^{(1)}\tilde{E}(t) + \chi^{(2)}\tilde{E}^2(t) + \chi^{(3)}\tilde{E}^3(t) + \cdots . \tag{4.2}$$

Thus the second-order nonlinear polarization, $\tilde{P}^{(2)}(t) = \chi^{(2)}\tilde{E}^2(t)$, created in the crystal by the optical field is given by

$$\tilde{P}^{(2)}(t) = 2\chi^{(2)}EE^* + \left(\chi^{(2)}E^2 e^{-i2\omega t} + \chi^{(2)}E^{*2}e^{i2\omega t}\right). \tag{4.3}$$

The second term in equation 4.3 consists of a contribution at frequency 2ω and can lead to generation of radiation at the second-harmonic frequency [103]. Physically, the origin of second-harmonic generation can be understood as an electromagnetic wave with frequency ω beating with itself in a nonlinear medium, thus producing a polarization at 2ω [104]. The efficiency of this process is critically dependent on the phase matching condition, as will be shown in the following.

We define the total electric field in the second-harmonic crystal [103] by:

$$\tilde{E}(z,t) = \tilde{E}_1(z,t) + \tilde{E}_2(z,t) \tag{4.4}$$
$$= E_1(z)e^{-i\omega_1 t} + E_2(z)_2 e^{-i\omega_2 t} + c.c. \tag{4.5}$$
$$= A_1(z)e^{-i(\omega_1 t + k_1 z)} + A_2(z)e^{-i(\omega_2 t + k_2 z)} + c.c., \tag{4.6}$$

where

$$E_j = E(\omega_j), \qquad j = 1, 2 \tag{4.7}$$
$$\omega_2 = 2\omega_1 \tag{4.8}$$
$$\omega_j = \frac{2\pi c}{\lambda_j} \tag{4.9}$$
$$k_j = \frac{n_j \omega_j}{c}, \quad n_j = \left[\varepsilon^{(1)}(\omega_j)\right]^{1/2}. \tag{4.10}$$

We can then formulate an expression for the amplitude change in the crystal [103]:

$$\frac{dA_2}{dz} = \frac{4\pi i \omega_2^2 d_{\text{eff}}}{k_2 c^2} A_1^2 e^{i\Delta k z}, \tag{4.11}$$

where d_{eff} is the effective nonlinear coefficient, and the wavevector mismatch is

$$\Delta k = 2k_1 - k_2. \tag{4.12}$$

Assuming undepleted pump ($A_1 = $ constant), we integrate equation 4.11 over the crystal length L, (from $z = 0$ to $z = L$) and find that the intensity of the second-harmonic field is expressed by

$$I_2 = \frac{128\pi^5 d_{\text{eff}}^2 I_1^2}{n_1^2 n_2 \lambda_2^2 c} L^2 \,\text{sinc}^2(\Delta k L/2). \tag{4.13}$$

Obviously the second-harmonic generation is most efficient when the phase mismatch

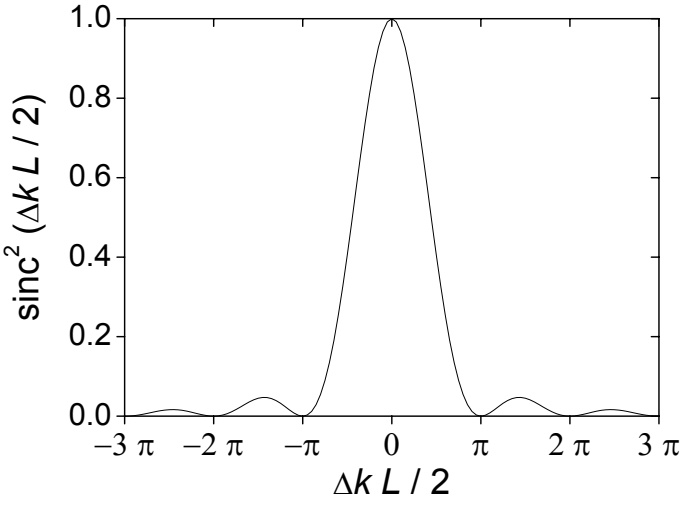

Figure 4.4: *Effect of phase mismatch factor on generation of second-harmonic signal.*

factor $sinc^2(\Delta kL/2)$ equals unity, i.e. when the phase-matching condition $\Delta k = 0$ is satisfied. The efficiency of the process decreases rapidly when $\Delta k \neq 0$, as can be seen from Figure 4.4. The physical origin of this effect can be traced to the fact that if the phase-matching condition is not met, the phases of the second-harmonic wavelets generated throughout the crystal are different and interfere destructively [105], thus preventing accumulation of the second-harmonic wave along the crystal. It is evident from equations 4.10 and 4.12 that to satisfy the phase-matching condition we must insist that $n(2\omega_1) = n(\omega_1)$. Since most optical materials present normal dispersion, i.e. $n(2\omega_1) > n(\omega_1)$, the phase-matching is commonly achieved using quasi phase-matching or birefringent phase-matching, where the birefringence of the crystal cancels out the dispersion.

For a given direction of propagation in a birefringent crystal, there are two linearly polarized plane waves that can propagate with different phase velocities, relating to two different refractive indices, namely the ordinary refractive index n_o and the extraordinary refractive index n_e. In a negative ($n_e < n_o$), uniaxial crystal such as BBO, the phase-matching condition then becomes

$$n_e(2\omega, \theta) = n_0(\omega), \tag{4.14}$$

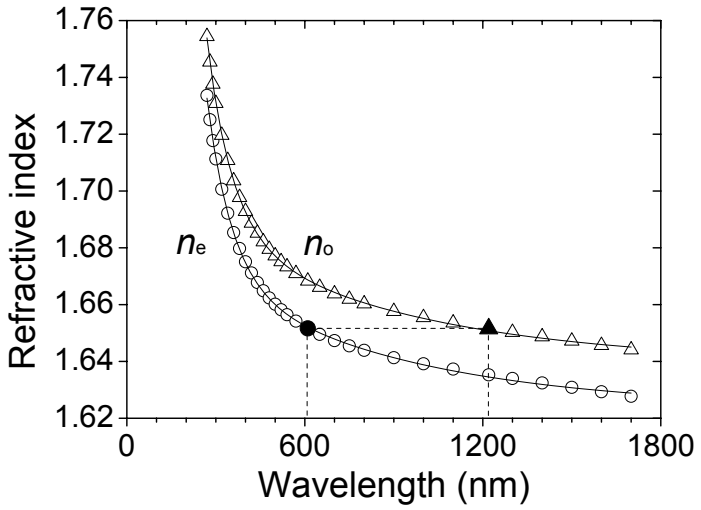

Figure 4.5: *Calculated ordinary (n_o) and extraordinary (n_e) refractive indices of BBO at propagation angle $\theta = 21^\circ$ at $T = 298$ K. Phase-matching is achieved at the fundamental wavelength $\lambda_1 = 1220$ nm* [106].

where θ is the propagation angle in regard to the crystal's optical axis (z-axis). Assuming sufficiently high birefringence, we may find a propagation angle where the ordinary refractive index of the fundamental wave equals the extraordinary refractive index of the second-harmonic wave, as illustrated in Figure 4.5. The concept of angular phase-matching in a uniaxial birefringent crystal is further explained in Figure 4.6 which presents the ordinary and extraordinary refractive indices in regard to the crystal's optical axis z and the wave propagation vector $\boldsymbol{k}$. Clearly, $n_o(\omega)$ and $n_o(2\omega)$ are constants, independent of θ, whereas $n_e(2\omega,\theta)$ can have values between its principle value $\bar{n}_e(2\omega)$ when $\theta = 90^\circ$, and $n_0(2\omega)$ when $\theta = 0^\circ$. By turning the crystal to a proper angle we can satisfy the phase-matching condition. From equation 4.14 we can also derive the expression [103]

$$\sin^2\theta = \frac{n_o(\omega)^{-2} - n_o(2\omega)^{-2}}{\bar{n}_e(2\omega)^{-2} - n_o(2\omega)^{-2}}, \tag{4.15}$$

from which the phase-matching angle can be conveniently calculated for a negative, uniaxial crystal with sufficient birefringent properties. For bi-axial birefringent crystals (such as LBO) we must also define a second propagation angle φ in an orthogonal

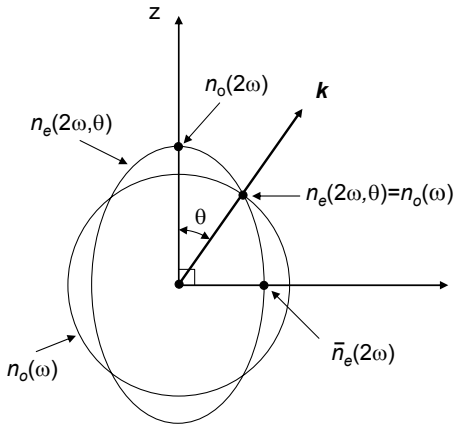

Figure 4.6: *Phase matching angle* θ *for type I second-harmonic generation in a negative uniaxial crystal such as BBO. Adopted from* [104].

plane. Since the phase-matching condition depends critically on the propagation angle, this phase-matching scheme is also called critical phase-matching. A disadvantage of critical phase-matching is that if $\theta \neq 90^\circ$ double refraction takes place in the crystal and the direction of energy flow for the second-harmonic beam is slightly different from θ [104]. Consequently we observe a *spatial walk-off* of the second-harmonic beam from the fundamental beam. Typically, spatial walk-off results in an elliptical shape of the second-harmonic output beam, but in the extreme case it could also lead to loss of spatial overlap of the two beams in a long crystal.

An alternative method to angular phase-matching is the so-called non-critical phase-matching (also called 90° phase-matching), where the beams are propagated along a crystal axis and the crystal temperature is adjusted in such a way that the phase velocities of the interacting beams are equal, i.e. $n_e(2\omega, 90^\circ) = n_o(\omega)$, for example. Non-critical phase-matching avoids spatial walk-off, but not all crystal materials or coatings can tolerate high temperatures or large thermal gradients. Therefore, heating of the crystal to the phase-matching temperature can be a very slow process. The phase-matching temperature may also be so far from room temperature as to be impractical.

Second-harmonic generation (critical or non-critical) uses either type I or type II scheme. Type I second-harmonic generation means that two beams with parallel di-

Table 4.1: *Nonlinear optical coefficients of selected optical crystal. Adopted from* [104]*, LBO after* [107].

Material	Formula	Nonlinear d coefficient relative to KDP	Transparency range (μm)	Damage threshold (GW/cm^2)
KDP	KH_2PO_4	$d_{36} = d_{14} = 1$	0.22–1.5	0.2
KTP	$KTiOPO_4$	$d_{31} = 13$	0.22–1.5	1
		$d_{32} = 10$		
		$d_{33} = 27.4$		
		$d_{24} = 15.2$		
		$d_{15} = 12.2$		
BBO	β-BaB_2O_4	$d_{22} = 4.1$	0.19–3	5
LBO	LiB_3O_5	$d_{31} = 2.4$	0.16–2.6	18.9
		$d_{32} = 2.2$		
Lithium niobate	$LiNbO_3$	$d_{31} = 12.5$	0.22–1.5	0.05
		$d_{22} = 6.35$		

rections of polarization produce a second-harmonic wave with orthogonal direction of polarization. Thus, we can denote $o_\omega + o_\omega \rightarrow e_{2\omega}$ and $e_\omega + e_\omega \rightarrow o_{2\omega}$. Type II second-harmonic generation means that beams with orthogonal directions of polarization produce the second-harmonic beam, i.e. $o_\omega + e_\omega \rightarrow e_{2\omega}$ or $o_\omega + e_\omega \rightarrow o_{2\omega}$.

The application and desired parameters (wavelength, nonlinear coefficient, damage threshold, walk-off, angular acceptance, hygroscopicity, etc.) determine the choice of crystal material. Some of the most common crystals are listed in Table 4.1. The desired properties may be very different for intra- and extracavity wavelength conversion. In the intracavity scheme the wavelength conversion takes place within a high-Q cavity, thus the light makes multiple passes through the crystal. In the extracavity conversion scheme the photons are passed through the crystal only once, which is why long crystals with high nonlinear coefficients are favored, as well as ultra-short pulses with high peak

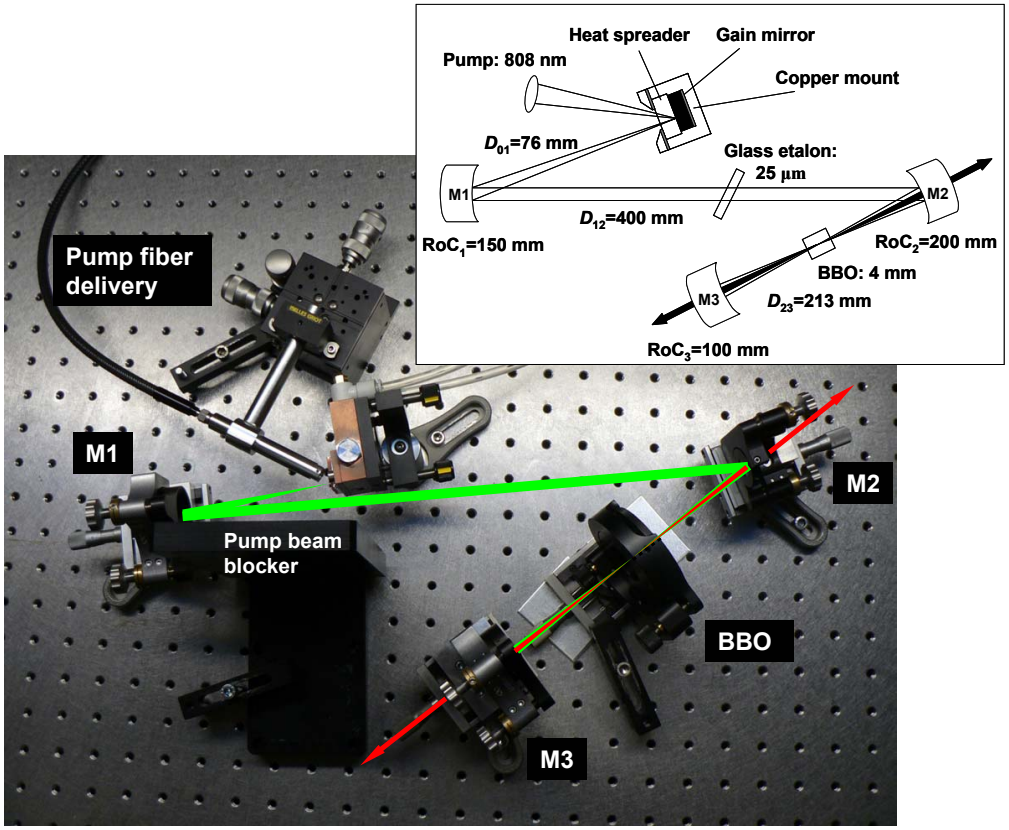

Figure 4.7: *Photograph of a typical Z-cavity used for SHG. Inset: schematics of the laser used for 615 nm second-harmonic generation. The green line represents 1230 nm radiation in the cavity and the red line represents 615 nm emission. RoC = Radius of curvature, D = distance between adjacent mirrors, BBO = β-barium borate crystal.*

power. In general, the intense optical field provided by laser sources enables highly efficient second-harmonic generation. Typically, the efficiency is on the order of some tens of percent, but may approach 100%.

4.3.2 Experimental

For the SHG experiment, the laser cavity was formed by the semiconductor gain mirror and three curved high reflective mirrors M1, M2, and M3, arranged in a Z-type configuration (Figure 4.7). M1 acts as a collimator, while M2 and M3 produce a focused

beam waist with diameter $2w_0 \approx 190\ \mu$m, and a Rayleigh range of $z_R \approx 23$ mm along the frequency-conversion crystal. The mirrors had a high reflectivity of $R \geq 99.8\%$ for the fundamental wavelength and a high transmission of $T \geq 90\%$ for the second-harmonic radiation. We used a 4-mm long, AR-coated, type-I, critically phase-matched, β-barium borate (BBO) crystal ($\theta = 21^\circ$, $\varphi = 90^\circ$) for nonlinear wavelength conversion to the red. The operation wavelength of the laser was controlled with a 25-μm thick uncoated Fabry–Pérot glass etalon placed in the cavity between mirrors M1 and M2. All measurements were performed at $T = 15\ ^\circ$C.

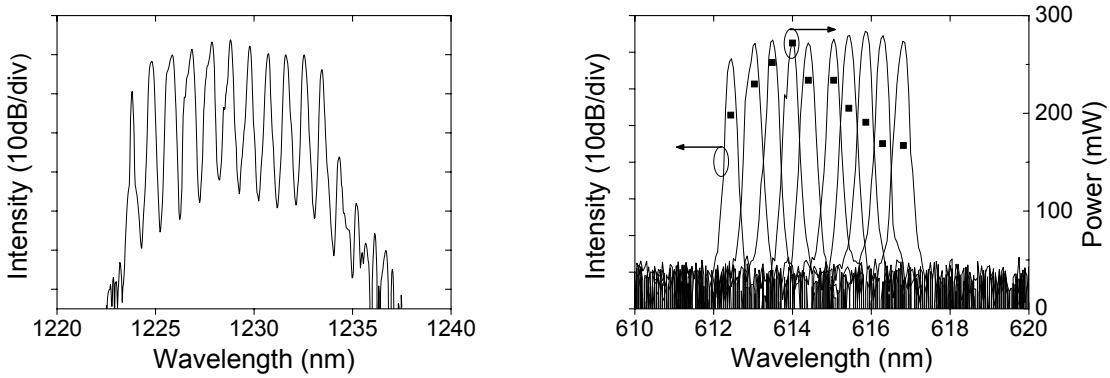

Figure 4.8: *(a) Free running laser spectrum without glass etalon or BBO crystal. (b) Tuning spectra of the frequency-doubled emission and corresponding output power at* $P_{\text{pump}} = 17$ *W.*

4.3.3 Results and discussion

Without the nonlinear crystal and the glass etalon, we observed a free running laser emission with multiple peaks around 1230 nm, as illustrated in Figure 4.8(a). Single narrow band emission peaks could be selected with the glass etalon. With the crystal and the etalon in place, strong red emission was observed from the laser. By tilting the etalon, the fundamental wavelength could be adjusted within a 9-nm spectral range, with discrete steps of about 1 nm, corresponding to the free spectral range of the diamond etalon. Consequently, a 4.5-nm tuning range from 612.5 nm to 617 nm was achieved for

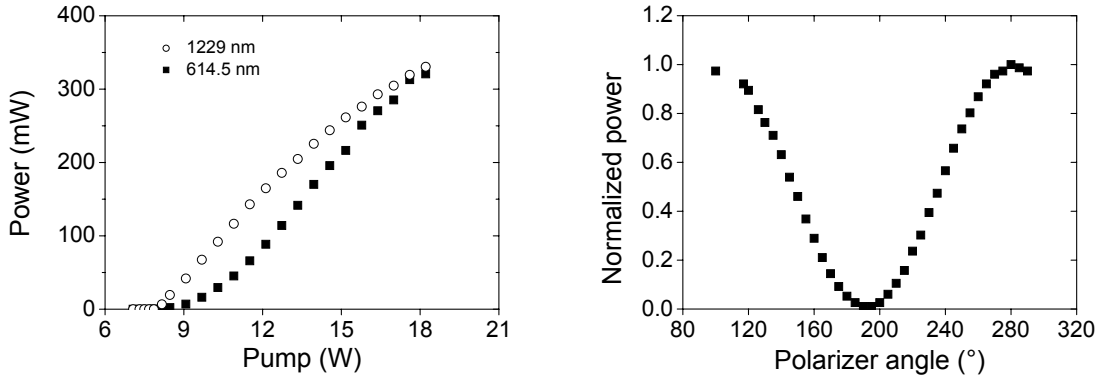

(a) (b)

Figure 4.9: *(a) Power at the fundamental and second-harmonic frequency (combined from outputs M2 and M3) given as a function of the incident pump power. (b) Normalized output power transmitted through a polarizer, given as a function of the polarizer angle.*

the red emission, as shown in Figure 4.8(b).

The fundamental and frequency-converted output beams were separated using low-loss prisms to perform independent power measurements. A maximum combined output power of 320 mW was observed at 614.5 nm with 18.2 W of pump power. The output powers from the single ports were 148 mW from M2 and 172 mW from M3. Light output characteristics for the red and residual IR emission are shown in Figure 4.9(a). The large amount (330 mW) of residual IR emission is likely a result of the large angle of the folding mirrors, that reduces their reflectivity. We did not observe saturation of the IR emission due to second-harmonic generation, but the output power at both visible and IR wavelengths was limited by the thermal roll-over. Based on the results presented in section 4.2.2, we estimated that the conversion efficiency from the IR to the visible was slightly over 20%. The total optical-to-optical conversion efficiency from 808 nm to 615 nm was about 1.7%, and the wall-plug efficiency about 1%. Polarization of the emission was measured using a polarizer and a power meter. Figure 4.9(b) presents the power transmitted through the polarizer as a function of the polarizer angle and confirms the linear state of polarization.

To summarize, we generated 320 mW of frequency-doubled 615 nm emission (Fig-

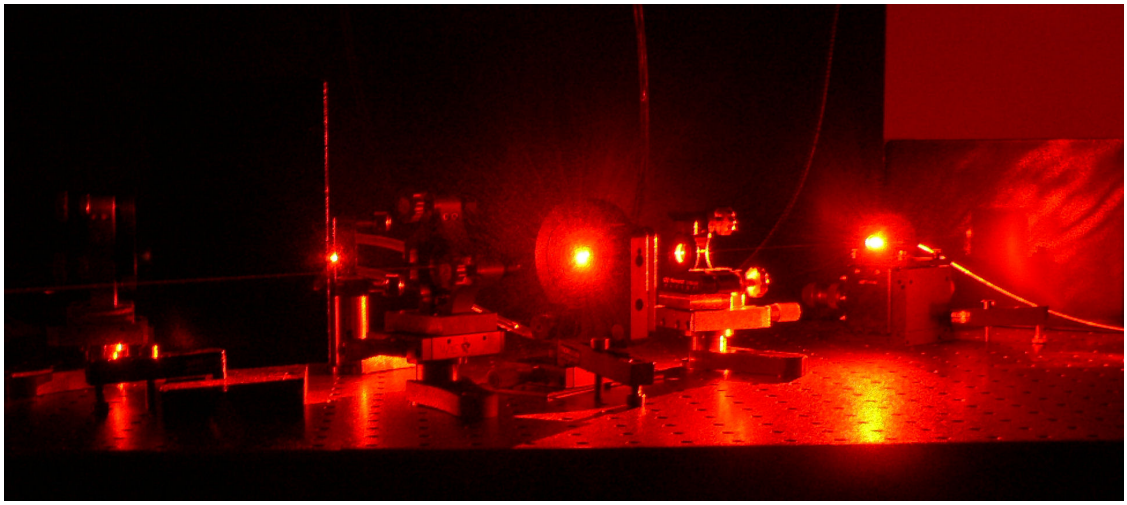

Figure 4.10: *Photograph of the frequency-doubled GaInNAs laser in operation. Courtesy of Lasse Orsila.*

ure 4.10) using an optically-pumped GaInNAs/GaAs-based disk laser that was capable of producing 1.46 W of power at the fundamental wavelength of 1230 nm. Although far from being optimized, the semiconductor gain structure used in this study still allowed for the best results at the time of publishing. By optimization of the laser cavity, HR mirrors, pumping, cooling, and overlap of the Fabry–Pérot resonance and the gain peak, the efficiency of the laser and second-harmonic generation was improved significantly at a later time by J. Rautiainen et al. [S5].

Chapter 5

GaSb disk laser emitting at 2025 nm

Gallium antimonide lasers form an important group of semiconductor lasers that operate at 2–5 μm wavelengths. The GaSb material system allows for the growth of high index contrast DBRs, which makes it highly interesting for vertical laser structures. In this chapter I describe the results obtained from a GaSb disk laser emitting at 2-μm.

5.1 Introduction

Significant research efforts have been directed to development of optoelectronic components based on gallium antimonides. The absorbtion lines of many important industrial gases and water vapor fall within the emission range of GaSb lasers [108, 109]. Therefore, optical spectroscopy and trace gas analysis are applications where GaSb lasers and detectors are expected to find a market. Other potential applications of these lasers include soft tissue laser surgery, remote sensing, LIDAR, infrared countermeasures, target illumination, optical pumping (Ho:YAG), etc.

Broad area edge-emitting GaSb lasers have been demonstrated with 1.7 W output power [110] and today high power single- and multi-emitters are commercially available at 2 μm. Tapered GaSb diode lasers have also been reported with high output power [111, 112]. Spectroscopic applications usually require a single-mode source with narrow band, preferably tunable, emission which has promoted the development of GaSb-based DFB lasers [113,114], coupled cavity lasers [115] and VCSELs [116,117] operating at various

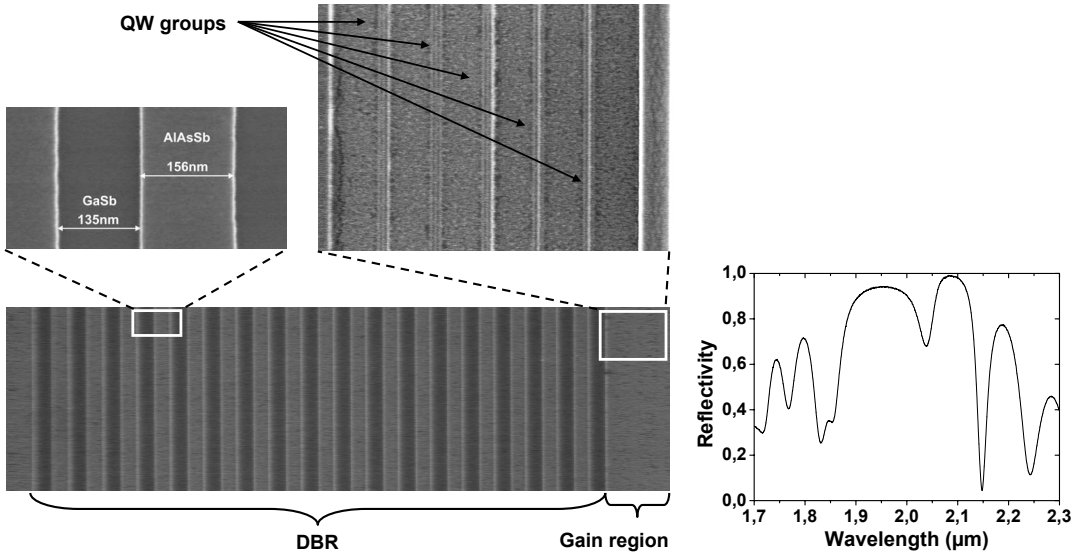

(a) (b)

Figure 5.1: *(a) SEM micrographs showing the 2-μm gain structure. (b) Reflectivity spectrum of the gain mirror. Courtesy of Karl Röβner.*

infrared wavelengths. Despite the fast development of edge-emitters and VCSEL, there existed only few reports on GaSb-based disk lasers [30, 31, 118] at the time when this research was started. The work presented here aimed to improve the previous results in terms of power and wavelength tuning.

5.2 Disk laser design and characterization

The MBE grown gain mirror was fabricated by the Technische Physik group of Universität Würzburg, Germany. The design included an 18-pairs GaSb/AlAsSb DBR and a gain region with 5 groups of 3 $Ga_{0.78}In_{0.22}Sb$ quantum wells with 8-nm thickness, placed in a 3λ-cavity [P3]. The layer structure is illustrated in detail in the micrographs of Figure 5.1(a). Owing to the high index contrast between the constituent DBR layers, the stopband spans over a broad wavelength range, as one can observe from Figure 5.1(b) showing the reflectivity spectrum of the gain mirror.

The gain mirror was processed in a similar manner as the GaInNAs laser described in

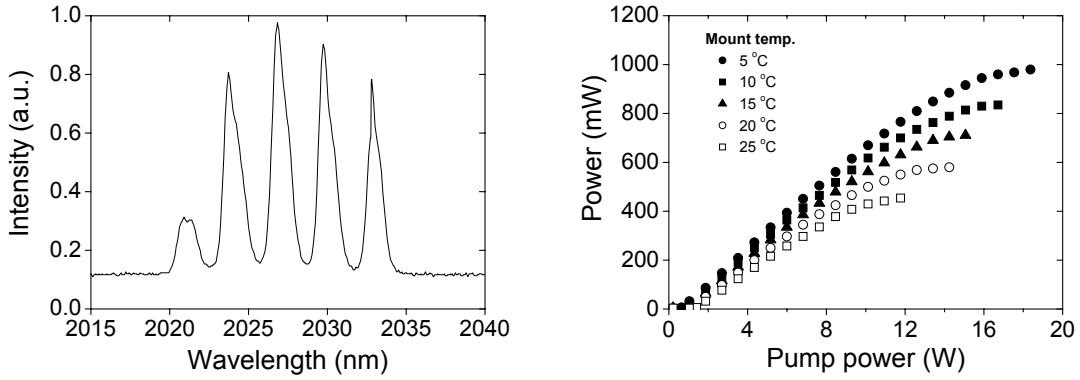

(a) (b)

Figure 5.2: *(a) Laser spectrum. (b) Light output characteristics at different mount temperatures, OC = 2%.*

the previous chapter and was used with a 300-μm thick type IIa diamond heatspreader. The V-shaped laser cavity included a 2% transmissive plane output coupler. The gain mirror was pumped with a 790-nm diode laser at an angle of 35° to the surface normal. The pump beam was focused to a spot of about $\varnothing = 180$ μm on the gain mirror. Free-running laser emission was observed at a wavelength near 2025 nm, Figure 5.2(a). The output characteristics were measured as a function of the mount temperature and the results obtained are presented in Figure 5.2(b). The measurements show strong dependence of the roll-over point and efficiency on the mount temperature. With moderate cooling of the mount temperature to 5 °C, we achieved a maximum output power of 1 W, and 700 mW at $T = 15$ °C. The output beam profile, measured with a 5-μm pinhole and photodetector and found to be Gaussian. The corresponding beam quality factor M^2, determined using the knife-edge technique, was less than 1.45.

5.2.1 Wavelength tuning

The broad DBR stopband and wide gain bandwidth of the semiconductor gain material suggested a potentially wide tuning range near 2 μm. The tunability was studied by inserting an uncoated single-element birefringent filter inside the laser resonator at

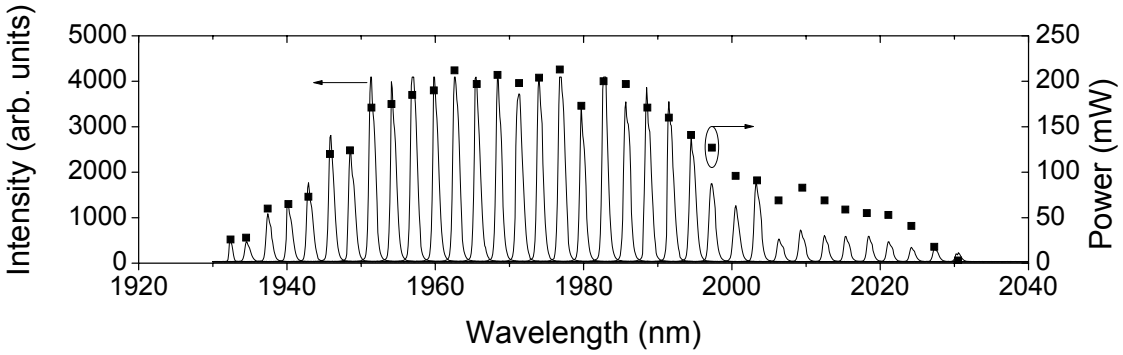

Figure 5.3: *Tuning spectra selected with a birefringent filter. The laser could be tuned from 1932 nm to 2030 nm with steps of 2.8 nm, by rotating the filter. The black dots represent the corresponding output power.*

the Brewster angle. By turning the filter, the operation wavelength could be tuned discretely with 2.8 nm steps. The tuning spectra at $T = 15$ °C, presented in Figure 5.3, show that lasing was obtained in the range of 1932–2030 nm, with output power varying from 3 mW to 213 mW. The observed Brewster loss was significant, over 100 mW at maximum power. Based on the previous results, it was expected that the filter also introduced a significant amount of other losses. To avoid any such losses, we assembled a self-seeded laser, where spectrally selective feedback was provided to the cavity by an external diffraction grating, as presented schematically in Figure 5.4.

Without optical feedback from the grating, the free-running wavelength was ob-

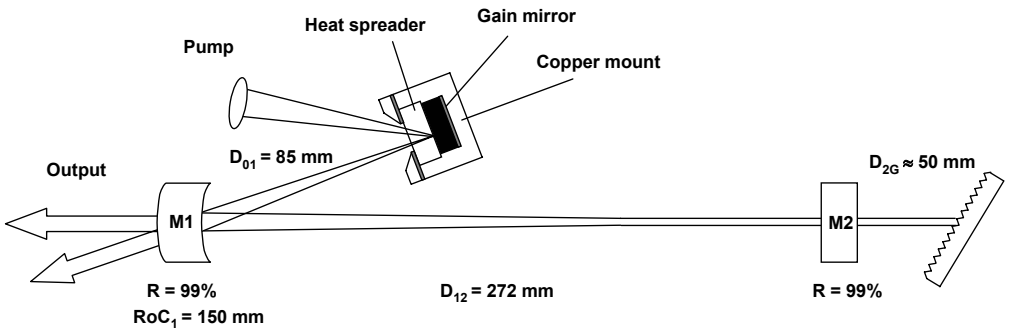

Figure 5.4: *Self-seeded laser configuration with an external diffraction grating.*

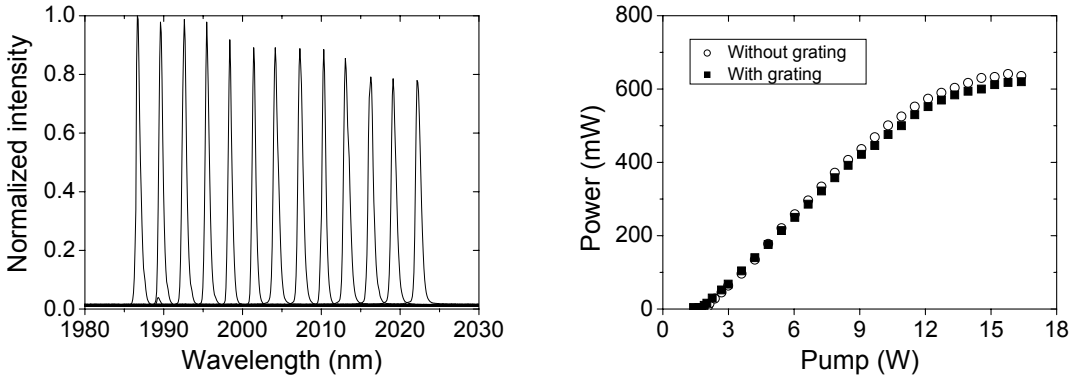

(a) (b)

Figure 5.5: *(a) Normalized tuning spectra obtained from the self-seeded laser. (b) Output characteristics with and without the diffraction grating. ($T = 15\ ^{\circ}C$).*

served around 2010 nm. The total output power, taken into account at all three outputs of mirrors M1 and M2, reached a maximum value of 640 mW. In the self-seeded regime, the power was collected from both outputs of mirror M2. By tilting the grating, we achieved tuning from 1987 to 2022 nm, as shown in Figure 5.5(a). The attempts to tune the wavelength beyond this range resulted in appearance of a free-running oscillation preventing further control of the spectrum by the seed signal. The light output characteristics with and without the seed signal, shown in Figure 5.5(b), reveal that self-seeded operation results in only a minor reduction in power. For the pump power of 15.8 W, the total power from the laser exceeded 500 mW across the tuning range [P4].

5.3 Conclusion

The results obtained from the GaSb disk laser demonstrate watt-level output power with good beam quality near room temperature. A tuning range of about 100 nm was achieved with an intracavity birefringent filter, although with reduced power. Use of a self-seeded tuning scheme allowed >0.5 W output in a 35-nm tuning range.

Chapter 6

Dual-wavelength disk laser for sum-frequency generation

This chapter deals with the generation of frequency-mixed radiation in a disk laser that operates simultaneously at two different wavelengths with large spectral separation. Although frequency-mixing in various lasers has been common for years, the concept of a frequency-mixed dual-wavelength SDL is new and allows for the control of the operation wavelengths by bandgap engineering. The laser concept, experimental and results are discussed.

6.1 Introduction

Dual-wavelength (and multi-wavelength) laser emission is desired for applications including WDM optical telecommunications, *sum-frequency generation* (SFG) [119], two-wavelength interferometry [120], and *difference-frequency generation* (DFG) [121]. The last mentioned application is particularly interesting, since it allows generation of *mid-infrared* (MIR) emission from near-infrared laser radiation. Coherent MIR emission can be obtained from optical parametric oscillators, quantum cascade lasers [122] or by mixing two laser beams for DFG [121]. The advantages of OPOs are high power and a superior tunability, but the systems are complex and expensive. Quantum cascade lasers, on the other hand, can be very compact, but their continuous wave power is lim-

ited at room temperature. The DFG systems incorporating ultrashort pulse lasers share the drawbacks of OPOs.

A compact, low-cost MIR source with reasonable output power at room temperature would be highly beneficial to many applications. Here we studied the semiconductor disk laser for generating intracavity frequency-converted radiation. Instead of DFG, the study was carried out using the SFG scheme for simplified measurements. However, the laser concept and requirements for the quality of the input beams are very similar for both SFG and DFG.

6.2 Multiple wavelength lasers

The key element to the experiment is a laser emitting simultaneously at two different wavelengths with significant spectral separation and comparable power. To date, several approaches have been employed to demonstrate dual-wavelength and multiple wavelength lasers based on fiber [123–125], solid state [126, 127] and semiconductor gain material. In semiconductors, these approaches used either an arrayed grating cavity design with physically separated gain media [128, 129], single broad band gain medium with an external grating and slit system [130, 131] or a coupled micro-cavity structure [132]. Within this work we utilized a semiconductor disk laser with monolithic dual-wavelength gain element and a common-cavity design that allows for large a spectral separation and offers the intriguing possibility for intracavity frequency-mixing.

6.2.1 Dual-wavelength disk laser

To ensure proper functioning of the dual-wavelength disk laser, the gain mirror was specially designed to provide independent pumping of the non-identical quantum wells and to minimize the cross-talk between the two signals. The gain mirror comprised a typical 29.5-pair AlAs/GaAs DBR, an 8 InGaAs QW gain region and an AlGaAs window layer. The gain region was divided into three subsections I–III, separated by wide bandgap AlAs carrier blocking layers, as illustrated in Figure 6.1. The purpose of this arrangement was to confine the photo-generated carriers within the AlAs boundaries and thus provide independent pumping of the QWs in each gain section. Sections I and

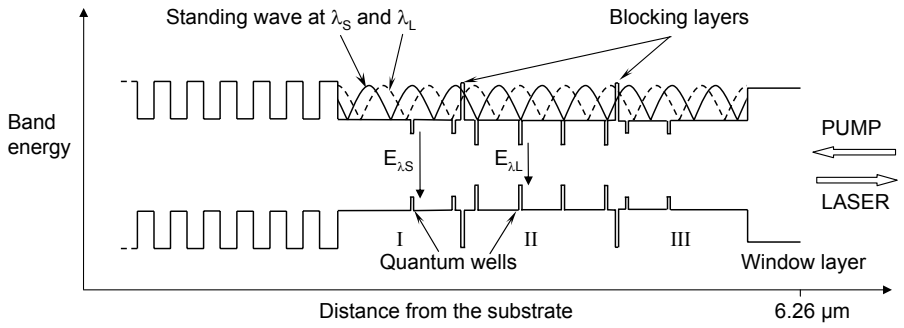

Figure 6.1: *Dual-wavelength laser gain structure.*

III contained two QWs, made of $In_{0.17}Ga_{0.83}As$ (QW_S), designed for emission at λ_S. Section II included four QWs of $In_{0.23}Ga_{0.77}As$ (QW_L), with emission at wavelength $\lambda_L > \lambda_S$. The QW_Ls were placed near the nodes of λ_S cavity mode to minimize their optical absorbtion at λ_S [S8]. The layer design and growth related issues of the dual-wavelength disk laser are described in detail in reference [72].

6.2.2 Laser performance

The dual-wavelength gain sample included a 300-μm thick capillary bonded diamond heat spreader with a TiO_2–SiO_2 AR coating. The sample was characterized in a typical V-shaped laser cavity using an 808-nm pump laser and a 1% transmissive output coupler. The measurements were carried out at 15 °C mount temperature. The output spectrum, presented in Figure 6.2(a), shows lasing at wavelengths of 984 nm and 1042 nm, thus yielding a spectral separation of 58 nm. The power characteristics at each wavelength were measured using a dual-head power meter and a dichroic beam splitter that enabled spatial separation of the co-axial beams. We obtained over 0.5 W of output at both wavelengths at about 9 W of pump power, as shown in Figure 6.2(b). For temporal measurements the signals were coupled into two equally long optical multi-mode fibers and analyzed using 1-GHz photodiodes and a 400-MHz dual-channel oscilloscope. We observed an output with a continuous wave component superimposed with chaotic self-pulsation. The quasi-sinusoidal pulsed components for the two signal were always observed to be in phase. An example of typical temporal output profiles is shown in Figure 6.3.

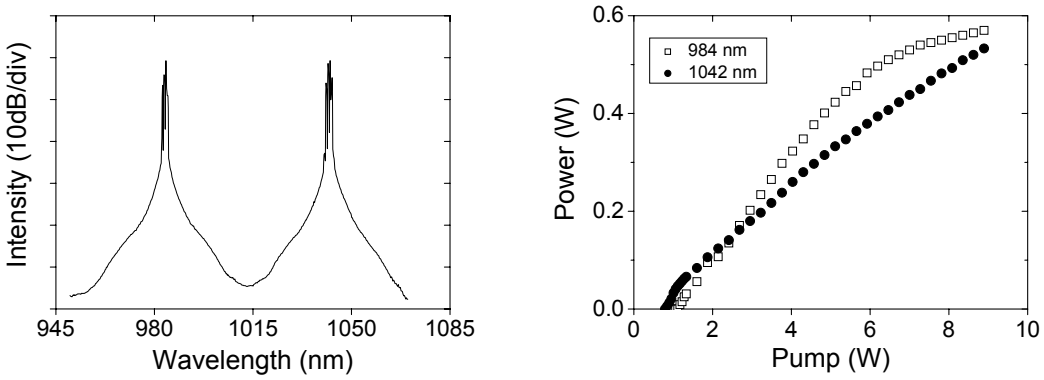

Figure 6.2: *(a) Dual-wavelength output spectrum showing laser emission near 984 nm and 1042 nm. (b) Output characteristics at 984 nm and 1042 nm, given as a function of incident 808 nm pump power ($T = 15\,^{\circ}C$, $OC = 1\%$).*

It should be noted, however, that the figure does not reveal the full essence of the self pulsation, as various pulse components with periods varying from ns to tens of ns could be observed by changing the trigger level. The self-pulsation could be suppressed to a certain extent by limiting the output at each wavelength to slightly over 100 mW. The pulse components were expected to rise from residual absorbtion of λ_S in the QW_Ls, which are not located exactly at the nodes of the λ_S's standing wave pattern. In the presence of residual absorbtion of λ_S, the pumping of λ_L at high power tends to follow the intensity variation of λ_S, possibly giving rise to in-phase oscillation of λ_L [S9]. However, this feature was not expected to disturb the process of frequency-conversion, due to a substantial cw component and the pulsed components having the same phase. The beam quality factor was measured with a scanning slit device and yielded a value of

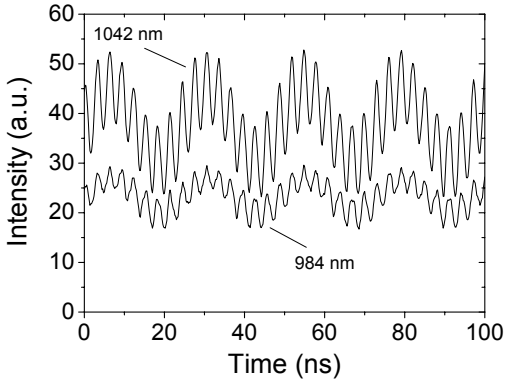

Figure 6.3: *An example of temporal profiles of the output signals.*

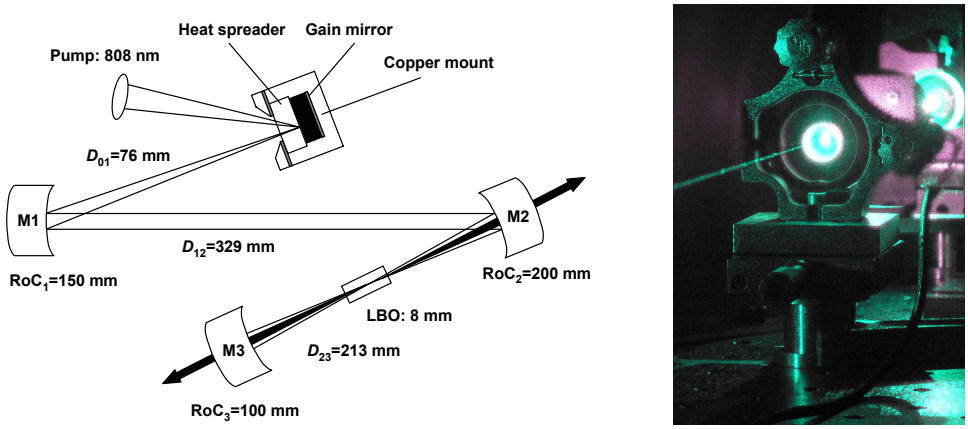

(a) (b)

Figure 6.4: *(a) Schematics of the Z-type laser cavity used for sum-frequency generation. (b) Photograph of the SFG output from M3.*

$M^2_{x,y} = 1.04$ for the output containing both co-axial beams.

6.3 Sum-frequency generation

Sum-frequency and difference-frequency generation are nonlinear conversion processes that involve two input waves at frequencies ω_1 and ω_2 interacting in a $\chi^{(2)}$ material to produce radiation at frequency $\omega_3 = \omega_1 + \omega_2$ (SFG), or $\omega_3 = \omega_1 - \omega_2$ (DFG). Thus second-harmonic generation is a degenerate case of sum-frequency generation. The wave vector mismatch for SFG is defined by $\Delta k = k_1 + k_2 - k_3$ and leads to a phase-matching condition $k_3 = k_1 + k_2$.

6.3.1 Experimental

The laser cavity used for the sum-frequency generation is shown in Figure 6.4(a). The curved mirrors M1–M3 had reflectivity $R \geq 99.8\%$ at the fundamental wavelengths, and transmission $T \geq 90\%$ for the sum-frequency emission. A 8-mm long, type-I, non-critically phase-matched lithium triborate (LBO) crystal ($\theta = 90°$,$\varphi = 0°$) was used for the sum-frequency generation. The crystal was placed in a thermo-controlled oven and

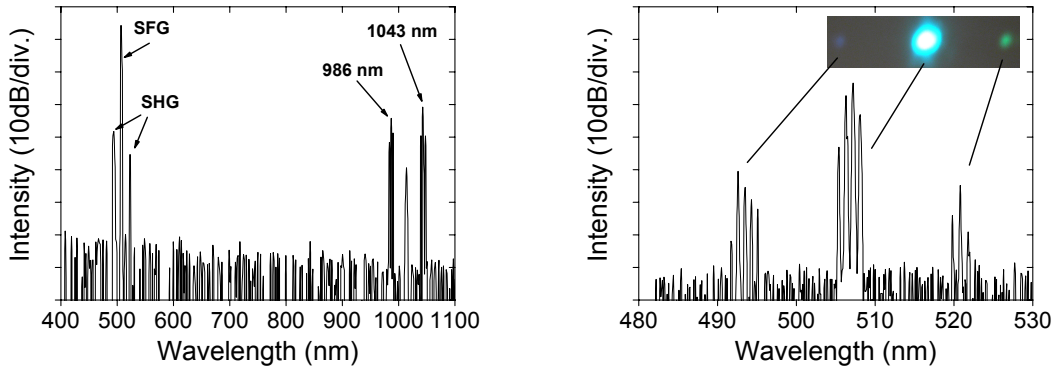

Figure 6.5: *(a) Output spectrum showing the laser emission and frequency-converted emission. (b) Spectrum of frequency-converted emission. Inset: photograph of the visible emission where different wavelengths are spatially separated with a diffraction grating.*

its temperature was kept at 212.5 °C for optimized phase-matching. The beam waist diameter $2w_0(\lambda_S) \approx 2w_0(\lambda_L)$ at the crystal was calculated to be about 200 μm with a Rayleigh range of $z_R = 34$ mm.

6.3.2 Results and discussion

Proper alignment of the laser cavity enabled low-threshold operation in the TEM_{00} mode for both IR wavelengths and resulted in strong aquamarine sum-frequency emission (Figure 6.4(b)), observed from mirrors M2 and M3. The optical spectrum, shown in Figure 6.5(a), reveals 3 visible and 3 infrared emission lines. Fundamental laser emission was observed near 986 nm and 1043 nm and the aquamarine SFG near 507 nm. Low intensity lines corresponding to poorly phase-matched second-harmonic generation are present at 493 nm and 521 nm, as shown in closer detail in Figure 6.5(b). An emission line at 1014 nm was also observed, although it was not present in the absence of the nonlinear crystal. The existence of this line was attributed to degenerate optical parametric amplification in the crystal that is located in a cavity with high Q-factor, and pumped by the sum-frequency emission.

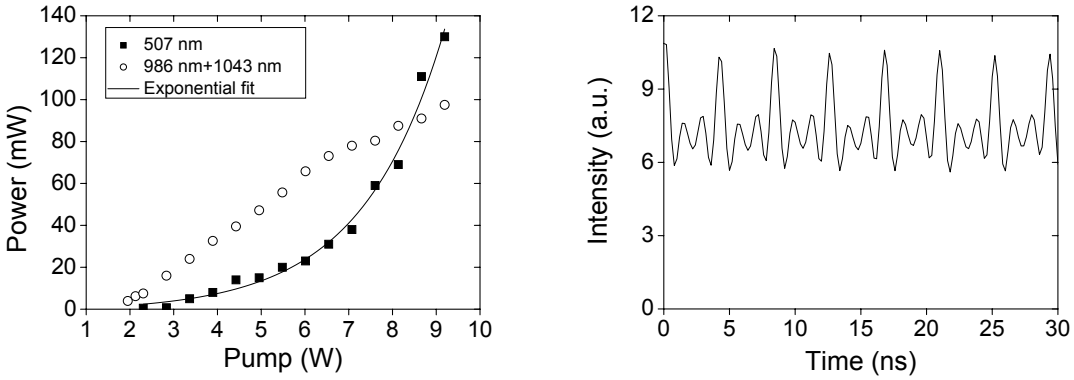

(a) (b)

Figure 6.6: *(a) Power of the sum-frequency emission and residual IR emission as a function of incident pump power from 808-nm diode laser. The curves present combined power from output ports M1, M2 and M3. (b) Temporal profile of the 507 nm sum-frequency output.*

The visible and IR beams were spatially separated with dichroic filters. Output characteristics of the IR and sum-frequency emission, presented in Figure 6.6(a), show that we obtained a total of 130 mW of continuous-wave sum-frequency emission at 9.2 W of pump power, yielding a total optical-to-optical conversion efficiency of about 1.4%. Based on the data shown in Figure 6.2(b), we estimated the conversion efficiency from IR to SFG to be on the order of 10%.

An Al-coated diffraction grating was used to resolve the visible colors spatially and allow the measurement of power at each wavelength separately. The power ratio was found to be 3:1000:1 for 493 nm, 507 nm, and 521 nm, respectively. Thus, the second-harmonic generation was negligible in comparison to the sum-frequency generation. The measurements of the IR laser beams yielded a power ratio of 0.35:1 for 986 nm and 1043 nm, respectively. The temporal profile of the sum-frequency emission was studied in a similar manner as for the dual-wavelength laser, discussed earlier. Chaotic self-pulsation behavior was not observed, but rather a continuous wave output with a stable AC-component superimposed, as presented in Figure 6.6(b).

The obtained results show that the two laser beams, overlapping in space, also overlap in the time domain to the extent that is required for efficient frequency-mixing. A

total of 130 mW of sum-frequency emission was achieved at 15 °C mount temperature. With a more optimized gain structure the power and spectral separation of the dual-wavelength laser can be further increased, as demonstrated in [133]. In comparison to designs deploying two pulsed lasers [121], or a laser with dual-gain elements in a single cavity [79], the proposed architecture with a monolithic gain element is significantly simpler and can be realized in a compact linear cavity suitable for commercial applications.

Based on the results presented here, it is reasonable to assume that the dual-wavelength disk laser concept could be further developed for intracavity difference-frequency generation to achieve coherent MIR emission. This would be a significant step towards creating a compact semiconductor based MIR source operating at room temperature with significant continuous wave output power.

Chapter 7

Conclusion

This thesis deals with processing and characterization of semiconductor disk lasers using InGaAs/GaAs, GaInNAs/GaAs and GaInSb/GaSb gain materials. The highlights of the thesis can be summarized by three main results.

The frequency-doubled GaInNaAs disk laser was used for generating high power 615 nm red emission, which is difficult to produce directly from the semiconductor material. The bandgap of the gain material can be easily tailored to generate amber-orange radiation by frequency-conversion. The proposed lasers could find use in RGB generation, medical and measurement related applications.

Within this work the output power of GaSb disk lasers was scaled to 1 W at a wavelength of 2 μm wavelength, showing the strong potential of this material system. Owing to the broad DBR stopband and gain bandwidth, the laser could be tuned over a span of about 100 nm with a birefringent filter. Low loss tuning in the 35 nm range was achieved using a self-seeded laser scheme.

In the last part of the thesis, the use of a dual-wavelength disk laser for generating frequency-mixed radiation was proposed and demonstrated. This novel laser concept used a nonlinear crystal for intracavity sum-frequency generation. The results obtained verified the spatial and temporal overlap of the ”two lasers” sharing a common cavity. This type of laser architecture could be used for difference-frequency generation of mid-infrared emission in the future.

Bibliography

[1] J.-Y. Kim, S. Cho, S.-J. Lim, J. Yoo, G. B. Kim, K.-S. Kim, J. Lee, S.-M. Lee, T. Kim, and Y. Park, "Efficient blue lasers based on gain structure optimizing of vertical-externalcavity surface-emitting laser with second harmonic generation," *Journal of Applied Physics*, vol. 101, p. 033103, 2007.

[2] J. Lee, S. Lee, T. Kim, and Y. Park, "7 W high-efficiency continuous-wave green light generation by intracavity frequency doubling of an end-pumped vertical external-cavity surface emitting semiconductor laser," *Applied Physics Letters*, vol. 89, p. 241107, 2006.

[3] S. Hilbich, W. R. Seelert, V. G. Ostroumov, C. Kannengiesser, R. von Elm, J. Mueller, E. S. Weiss, H. Zhou, and J. L. A. Chilla, "New wavelengths in the yellow orange range between 545 nm and 580 nm generated by intracavity frequency-doubled optically pumped semiconductor lasers," in *Proc. Photonics West 2007, Solid State Lasers XVI: Technology and Devices, SPIE 6451-10*, 2007.

[4] W. B. Jiang, S. R. Friberg, H. Iwamura, and Y. Yamamoto, "High powers and sub-picosecond pulses from an external-cavity surface-emitting InGaAs/InP multiple quantum well laser," *Applied Physics Letters*, vol. 58, no. 8, pp. 807–809, 1991.

[5] H. Q. Le, S. D. Cecca, and A. Mooradian, "Scalable high-power optically pumped GaAs laser," *Applied Physics Letters*, vol. 58, no. 18, pp. 1967–1969, 1991.

[6] W. H. Xiang, S. R. Friberg, K. Watanabe, S. Machida, Y. Sakai, H. Iwamura, and Y. Yamamoto, "Sub-100 femtosecond pulses from an external-cavity surface-

emitting lnGaAs/InP multiple quantum well laser with soliton-effect compression," *Applied Physics Letters*, vol. 59, no. 17, pp. 2076–2078, 1991.

[7] W. B. Jiang, R. Mirin, and J. E. Bowers, "Mode-locked GaAs vertical cavity surface emitting lasers," *Applied Physics Letters*, vol. 60, no. 6, pp. 677–679, 1992.

[8] D. C. Sun, S. R. Friberg, K. Watanabe, S. Machida, Y. Horikoshiand, and Y. Yamamoto, "High power and high efficiency vertical cavity surface emitting GaAs laser," *Applied Physics Letters*, vol. 61, no. 13, pp. 1502–1503, 1992.

[9] M. Kuznetsov, F. Hakimi, R. Sprague, and A. Mooradian, "High-power (>0.5-W CW) diode-pumped vertical-external-cavity surface-emitting semiconductor lasers with circular TEM_{00} beams," *IEEE Photonics Technology Letters*, vol. 9, no. 8, pp. 1063–1065, 1997.

[10] S. Lutgen, T. Albrecht, P. Brick, W. Reill, J. Luft, and W. Späth, "8-W high-efficiency continuous-wave semiconductor disk laser at 1000 nm," *Applied Physics Letters*, vol. 82, no. 21, pp. 3620–3622, 2003.

[11] J. Chilla, S. Butterworth, A. Zeitschel, J. Charles, A. Caprara, M. Reed, and L. Spinelli, "High-power optically pumped semiconductor lasers," in *Proc. Photonics West 2004, Solid State Lasers XIII: Technology and Devices, SPIE 5332*, 2004, pp. 143–150.

[12] C. Stewen, K. Contag, M. Larionov, A. Giesen, and H. Hügel, "A 1-kW CW thin disc laser," *IEEE Journal of Selected Topics in Quantum Electronics*, vol. 6, no. 4, pp. 650–657, 2000.

[13] E. J. Saarinen, A. Härkönen, S. Suomalainen, and O. G. Okhotnikov, "Power scalable semiconductor disk laser using multiple gain cavity," *Optics Express*, vol. 14, no. 26, pp. 12 868–12 871, 2006.

[14] L. Fan, M. Fallahi, J. Hader, A. R. Zakharian, J. V. Moloney, R. Bedford, W. Stolz, and S. W. Koch, "Multichip vertical-external-cavity surface-emitting lasers: a coherent power scaling scheme," *Optics Letters*, vol. 31, no. 24, pp. 3612–3614, 2006.

[15] L. E. Hunziker, Q. Shu, C. Ihli, G. J. Mahnke, M. Rebut, J. L. A. Chilla, A. L. Caprara, H. Zhou, E. S. Weiss, and M. K. Reed, "Power-scaling of optically pumped semiconductor lasers," in *Proc. Photonics West 2007, Solid State Lasers XVI: Technology and Devices, SPIE 6451-09*, 2007.

[16] M. Kuznetsov, F. Hakimi, R. Sprague, and A. Mooradian, "Design and characteristics of high-power (>0.5-W CW) diode-pumped vertical-external-cavity surface-emitting semiconductor lasers with circular TEM_{00} beams," *IEEE Journal of Selected Topics in Quantum Electronics*, vol. 5, no. 3, pp. 561–573, 1999.

[17] J. E. Hastie, L. G. Morton, S. Calvez, M. D. Dawson, T. Leinonen, M. Pessa, G. Gibson, and M. J. Padgett, "Red microchip VECSEL array," *Optics Express*, vol. 13, no. 8, pp. 7209–7214, 2005.

[18] S.-H. Park, J. Kim, H. Jeon, T. Sakong, S.-N. Lee, S. Chae, Y. Park, C.-H. Jeong, G.-Y. Yeom, and Y.-H. Cho, "Room-temperature GaN vertical-cavity surface-emitting laser operation in an extended cavity scheme," *Applied Physics Letters*, vol. 83, pp. 2121–2123, 2003.

[19] M. I. Müller, N. Linder, C. Karnutsch, W. Schmid, K. Streubel, J. Luft, S. S. Beyertt, A. Giesen, and G. H. Dohler, "Optically pumped semiconductor thin-disk laser with external cavity operating at 660 nm," in *Proc. Vertical-Cavity Surface-Emitting Lasers VI, SPIE 4649*, 2002, pp. 265–271.

[20] J. E. Hastie, S. Calvez, M. D. Dawson, T. Leinonen, A. Laakso, J. Lyytikäinen, and M. Pessa, "High power CW red VECSEL with linearly polarized TEM_{00} output beam," *Optics Express*, vol. 13, no. 1, pp. 77–81, 2005.

[21] J. E. Hastie, J.-M. Hopkins, S. Calvez, C. W. Jeon, D. Burns, R. Abram, E. Riis, A. I. Ferguson, and M. D. Dawson, "0.5-W single transverse-mode operation of an 850-nm diode-pumped surface-emitting semiconductor laser," *IEEE Photonics Technology Letters*, vol. 15, no. 7, pp. 894–896, 2003.

[22] S. J. McGinily, R. H. Abram, K. S. Gardner, E. Riis, A. I. Ferguson, and J. S. Roberts, "Novel gain medium design for short-wavelength vertical-external-

cavity surface-emitting laser," *IEEE Journal of Quantum Electronics*, vol. 43, no. 6, pp. 445–450, 2007.

[23] S.-S. Beyertt, U. Brauch, F. Demaria, N. Dhidah, A. Giesen, T. Kübler, S. Lorch, F. Rinaldi, and P. Unger, "Efficient gallium-arsenide disk laser," *IEEE Journal of Quantum Electronics*, vol. 43, no. 10, pp. 869–875, 2007.

[24] K.-S. Kim, J. Yoo, G. Kim, S. Lee, S. Cho, J. Kim, T. Kim, and Y. Park, "920-nm vertical-external-cavity surface-emitting lasers with a slope efficiency of 58% at room temperature," *IEEE Photonics Technology Letters*, vol. 19, no. 20, pp. 1655–1657, 2007.

[25] L. Fan, C. Hessenius, M. Fallahi, J. Hader, H. Li, J. V. Moloney, W. Stolz, and S. W. Koch, "Highly strained InGaAs/GaAs multiwatt vertical-external-cavity surface-emitting laser emitting around 1170 nm," *Applied Physics Letters*, vol. 91, p. 131114, 2007.

[26] J.-M. Hopkins, S. Smith, C. Jeon, H. Sun, D. Burns, S. Calvez, M. Dawson, T. Jouhti, and M. Pessa, "0.6 W CW GaInNAs vertical external-cavity surface emitting laser operating at 1.32 μm," *IET Electronics Letters*, vol. 40, no. 1, pp. 30–31, 2004.

[27] C. Symonds, I. Sagnes, A. Garnache, S. Hoogland, G. Saint-Girons, A. C. Tropper, and J.-L. Oudar, "Continuous-wave operation of monolithically grown 1.55 μm optically pumped vertical-external-cavity surface-emitting lasers," *Applied Optics*, vol. 42, no. 33, pp. 6678–6681, 2003.

[28] C. Symonds, J. Dion, I. Sagnes, M. Dainese, M. Strassner, L. Leroy, and J.-L. Oudar, "High performance 1.55 μm vertical external cavity surface emitting laser with broadband integrated dielectric-metal mirror," *IET Electronics Letters*, vol. 40, no. 12, pp. 734–735, 2004.

[29] H. Lindberg, M. Strassner, E. Gerster, and A. Larsson, "0.8 W optically pumped vertical external cavity surface emitting laser operating CW at 1550 nm," *IET Electronics Letters*, vol. 40, no. 10, pp. 601–602, 2004.

[30] L. Cerutti, A. Garnache, E. Genty, A. Ouvrard, and C. Alibert, "Low threshold, room temperature laser diode pumped Sb-based VECSEL emitting around 2.1 μm," *IET Electronics Letters*, vol. 39, no. 3, pp. 290–292, 2003.

[31] N. Schulz, M. Rattunde, C. Manz, K. Köhler, C. Wild, J. Wagner, S. Beyertt, S, U. Brauch, T. Kübler, and A. Giesen, "High power continuous wave operation of a GaSb-based VECSEL emitting near 2.3 μm," *Physica Status Solidi(c)*, vol. 3, pp. 386–390, 2006.

[32] S. Giet, H. D. Sun, S. Calvez, M. D. Dawson, S. Suomalainen, A. Härkönen, M. Guina, O. Okhotnikov, and M. Pessa, "Spectral narrowing and locking of a vertical-external-cavity surface-emitting laser using an intracavity volume Bragg grating," *IEEE Photonics Technology Letters*, vol. 18, no. 16, pp. 1786–1788, 2006.

[33] M. A. Holm, D. Burns, A. I. Ferguson, and M. D. Dawson, "Actively stabilized single-frequency vertical-external-cavity AlGaAs laser," *IEEE Photonics Technology Letters*, vol. 11, no. 12, pp. 1551–1553, 1999.

[34] H. Lindberg, A. Larsson, and M. Strassner, "Single-frequency operation of a high-power long-wavelength semiconductor disk laser," *Optics Letters*, vol. 30, no. 17, pp. 2260–2262, 2005.

[35] L. Fan, M. Fallahi, A. R. Zakharian, J. Hader, J. V. Moloney, R. Bedford, J. T. Murray, W. Stolz, and S. W. Koch, "Extended tunability in a two-chip VECSEL," *IEEE Photonics Technology Letters*, vol. 19, no. 8, pp. 544–546, 2007.

[36] J. E. Hastie, L. G. Morton, A. J. Kemp, M. D. Dawson, A. B. Krysa, and J. S. Roberts, "Tunable ultraviolet output from an intracavity frequency-doubled red vertical-external-cavity surface-emitting laser," *Applied Physics Letters*, vol. 89, p. 061114, 2006.

[37] K. S. Kim, J. R. Yoo, S. H. Cho, S. M. Lee, S. J. Lim, J. Y. Kim, J. H. Lee, T. Kim, and Y. J. Park, "1060 nm vertical-external-cavity surface-emitting lasers with an

optical-to-optical efficiency of 44% at room temperature," *Applied Physics Letters*, vol. 88, p. 091107, 2006.

[38] N. Schulz, M. Rattunde, C. Ritzenthaler, B. Rösener, C. Manz, K. Köhler, J. Wagner, and U. Brauch, "Resonant optical in-well pumping of an (AlGaIn)(AsSb)-based vertical-external-cavity surface-emitting laser emitting at 2.35 μm," *Applied Physics Letters*, vol. 91, p. 091113, 2007.

[39] U. Keller and A. C. Tropper, "Passively modelocked surface-emitting semiconductor lasers," *Physics Reports*, vol. 429, no. 2, pp. 67–120, 2006.

[40] S. Hoogland, A. Garnache, I. Sagnes, J. S. Roberts, and A. C. Tropper, "10-GHz train of sub-500-fs optical soliton-like pulses from a surface-emitting semiconductor laser," *IEEE Photonics Technology Letters*, vol. 17, no. 2, pp. 267–269, 2005.

[41] D. Lorenser, D. J. H. C. Maas, H. J. Unold, A.-R. Bellancourt, B. Rudin, E. Gini, D. Ebling, and U. Keller, "50-GHz passively mode-locked surface-emitting semiconductor laser with 100-mW average output power," *IEEE Journal of Quantum Electronics*, vol. 42, no. 8, pp. 838–847, 2006.

[42] A. Aschwanden, D. Lorenser, H. J. Unold, R. Paschotta, E. Gini, and U. Keller, "2.1-W picosecond passively mode-locked external-cavity semiconductor laser," *Optics Letters*, vol. 30, no. 3, pp. 272–274, 2005.

[43] D. Maas, A.-R. Bellancourt, B. Rudin, M. Golling, H. Unold, T. Südmeyer, and U. Keller, "Vertical integration of ultrafast semiconductor lasers," *Applied Physics B*, vol. 88, pp. 493–497, 2007.

[44] W. Zhang, T. Ackemann, S. McGinily, M. Schmid, E. Riis, and A. I. Ferguson, "Operation of an optical in-well-pumped vertical-external-cavity surface-emitting laser," *Applied Optics*, vol. 45, no. 29, pp. 7729–7735, 2006.

[45] N. Yokouchi, T. Miyarnoto, T. Uchida, Y. Inaba, F. Koyama, and K. Iga, "40 Å continuous tuning of a GaInAsP/InP vertical-cavity surface-emitting laser using

an external mirror," *IEEE Photonics Technology Letters*, vol. 4, no. 7, pp. 701–703, 1992.

[46] M. A. Hadley, G. C. Wilson, K. Y. Lau, and J. S. Smith, "High single-transverse-mode output from external-cavity surface-emitting laser diodes," *Applied Physics Letters*, vol. 63, no. 12, pp. 1607–1609, 1993.

[47] J. McInerney, A. Mooradian, A. Lewis, A. Shchegrov, E. Strzelecka, D. Lee, J. Watson, M. Liebman, G. Carey, B. Cantos, W. Hitchens, and D. Heald, "High-power surface emitting semiconductor laser with extended vertical compound cavity," *IET Electronics Letters*, vol. 39, no. 39, pp. 523–525, 2003.

[48] A. Strittmatter, T. D. Germann, J. Pohl, U. W. Pohl, D. Bimberg, J. Rautiainen, M. Guina, and O. G. Okhotnikov, "1040 nm vertical external cavity surface emitting laser based on InGaAs quantum dots grown in Stranski–Krastanow regime," *IET Electronics Letters*, vol. 44, no. 4, pp. 290–291, 2008.

[49] H. A. Macleod, *Thin-film optical filters*, 3rd ed. Bristol and Philadelphia: Institute of Physics Publishing, 2001.

[50] P. Savolainen, "Puolijohdelasereiden peilipäätyjen pinnoitus," Master's thesis, Tampere University of Technology, 1992.

[51] E. D. Palik, *Handbook of Optical Constants of Solids*. San Diego, CA: Academic Press, 1985.

[52] M. Reddy, T. Asano, R. Koda, D. Buell, and L. Coldren, "Molecular beam epitaxy-grown AIGalnAs/lnP distributed Bragg reflectors for 1.55 μm VCSELs," *IET Electronics Letters*, vol. 38, no. 20, pp. 1181–1182, 2002.

[53] M. M. Uribe, C. E. M. de Oliveira, J. H. Clerice, R. S. Miranda, M. B. Zakia, M. M. G. de Carvalho, and N. B. Patel, "Measurement of refractive index of GaSb (1.8 to 2.56 μm) using a prism," *IET Electronics Letters*, vol. 32, p. 262, 1996.

[54] R. E. Fern and A. Onton, "Refractive index of AlAs," *Journal of Applied Physics*, vol. 42, no. 9, pp. 3499–3500, 1971.

[55] G. Rempe, R. J. Thompson, H. J. Kimble, and R. Lalezari, "Measurement of ultralow losses in an optical interferometer," *Optics Letters*, vol. 17, no. 5, pp. 363–365, 1992.

[56] L. Orsila, "Interferometric dielectric reflectors for dispersion compensation in fibre lasers," Master's thesis, Tampere University of Technology, Tampere, 2003.

[57] S. W. Corzine, R. S. Geels, J. W. Scott, R. H. Yan, and L. A. Coldren, "Design of Fabry-Perot surface-emitting lasers with a periodic gainstructure," *IEEE Journal of Quantum Electronics*, vol. 25, no. 6, pp. 1513–1524, 1989.

[58] G. A. Keeler, D. K. Serkland, K. M. Geib, G. M. Peake, and A. Mar, "Single transverse mode operation of electrically pumped vertical-external-cavity surface-emitting lasers with micromirrors," *IEEE Photonics Technology Letters*, vol. 17, no. 3, pp. 522–524, 2005.

[59] A. C. Tropper, "VECSELs," in *Proc. International Summer School - New Frontiers in Optical Technologies*. Tampere University of Technology, Tampere, Finland, 2003.

[60] J. Yoo, K. Kim, S. Lee, S. Lim, G. Kim, J. Kim, S. Cho, J. Lee, T. Kim, and Y. Park, "Gain structure optimization of vertical external cavity surface emitting laser at 920 nm," *Applied Physics Letters*, vol. 89, p. 131125, 2006.

[61] F. Saas, V. Talalaev, U. Griebner, J. W. Tomma, M. Zorn, A. Knigge, and M. Weyers, "Optically pumped semiconductor disk laser with graded and step indices," *Applied Physics Letters*, vol. 89, p. 151120, 2006.

[62] A. K. Salokatve and J. L. A. Chilla, "US patent 6,327,293: Optically-pumped external-mirror vertical-cavity semiconductor-laser," Coherent Inc., Santa Clara, CA, 1998.

[63] N. L. Bazhenov, K. D. Mynbaev, V. I. Ivanov-Omskii, V. A. Smirnov, V. P. Evtikhiev, N. A. Pikhtin, M. G. Rastegaeva, A. L. Stankevich, I. S. Tarasov, A. S. Shkolnik, and G. G. Zegrya, "Temperature dependence of the threshold current of QW lasers," *Semiconductors*, vol. 39, no. 10, pp. 1210–1214, 2005.

[64] R. Fehse, S. Sweeney, A. Adams, D. McConville, H. Riechert, and L. Geelhaar, "Influence of growth temperature on carrier recombination in GaInNAs-based lasers," *IEE Proceedings Optoelectronics*, vol. 151, no. 5, pp. 447–451, 2004.

[65] A. J. Kemp, R. S. Conroy, G. J. Friel, and B. D. Sinclair, "Guiding effects in Nd:YVO_4 microchip lasers operating well above threshold," *IEEE Journal of Quantum Electronics*, vol. 35, no. 4, pp. 675–681, 1999.

[66] A. R. Zakharian, J. Hader, J. V. Moloney, S. W. Koch, P. Brick, and S. Lutgen, "Experimental and theoretical analysis of optically pumped semiconductor disk lasers," *Applied Physics Letters*, vol. 83, no. 7, pp. 1313–1315, 2003.

[67] R. Häring, R. Paschotta, A. Aschwanden, E. Gini, F. Morier-Genoud, and U. Keller, "High-power passively mode-locked semiconductor lasers," *IEEE Journal of Quantum Electronics*, vol. 38, no. 9, pp. 1268–1275, 2002.

[68] H. Lindberg, M. Strassner, E. Gerster, J. Bengtsson, and A. Larsson, "Thermal management of optically pumped long-wavelength InP-based semiconductor disk lasers," *IEEE Journal of Selected Topics in Quantum Electronics*, vol. 11, no. 5, pp. 1126–1134, 2005.

[69] A. J. Kemp, G. J. Valentine, J.-M. Hopkins, J. E. Hastie, S. A. Smith, S. Calvez, M. D. Dawson, and D. Burns, "Thermal management in vertical-external-cavity surface-emitting lasers: Finite-element analysis of a heatspreader approach," *IEEE Journal of Quantum Electronics*, vol. 41, no. 2, pp. 148–155, 2005.

[70] W. J. Alford, T. D. Raymond, and A. A. Allerman, "High power and good beam quality at 980 nm from a vertical external-cavity surface-emitting laser," *Journal of Optical Society America B*, vol. 19, no. 4, pp. 663–666, 2002.

[71] R. Häring, "Miniature pulsed laser sources: repetition rates from kilohertz to gigahertz," Ph.D. dissertation, Swiss Federal Institute of Technology, Zürich, Switzerland, 2001.

[72] T. Leinonen, "The design and fabrication of lasing semiconductor nanostructures employing vertical-cavity geometry," Ph.D. dissertation, Tampere University of Technology, Tampere, Finland, 2007.

[73] E. Yablonovitch, D. Hwang, T. J. Gmitter, L. T. Flores, and J. P. Harbison, "Van der Waals bonding of epitaxial liftoff films on to arbitrary substrates," *Applied Physics Letters*, vol. 56, no. 24, pp. 2419–2421, 1990.

[74] Z. L. Liau, "Semiconductor wafer bonding via liquid capillarity," *Applied Physics Letters*, vol. 77, no. 5, pp. 651–653, 2000.

[75] E. Hecht, *Optics*, 3rd ed. Massachusetts: Addison-Wesley, 1998.

[76] A. M. Zaitsev, *Optical properties of diamond*. Berlin Heidelberg: Springer-Verlag, 2001.

[77] F. van Loon, A. J. Kemp, A. J. Maclean, S. Calvez, J.-M. Hopkins, J. E. Hastie, M. D. Dawson, and D. Burns, "Intracavity diamond heatspreaders in lasers: the effects of birefringence," *Optics Express*, vol. 14, no. 20, pp. 9250–9260, 2006.

[78] E. Gerster, I. Ecker, S. Lorch, C. Hahn, S. Menzel, and P. Unger, "Orange-emitting frequency-doubled GaAsSb/GaAs semiconductor disk laser," *Journal of Applied Physics*, vol. 94, no. 12, pp. 7397–7401, 2003.

[79] H. M. Kretschmann, F. Heine, G. Huber, and T. Halldórsson, "All-solid-state continuous-wave doubly resonant all-intracavity sum-frequency mixer," *Optics Letters*, vol. 22, no. 19, pp. 1461–1463, 1997.

[80] S. M. Giffin, I. T. McKinnie, and V. V. Ter-Mikirtychev, "Tunable visible solid-state lasers based on second-harmonic generation of LiF:F_2^- in potassium titanyl phosphate," *Optics Letters*, vol. 23, no. 3, pp. 192–194, 1998.

[81] J.-P. Debray, N. Bouché, G. L. Roux, R. Raj, and M. Quillec, "Monolithic vertical cavity device lasing at 1.55 μm in InGaAlAs system," *IET Electronics Letters*, vol. 33, no. 10, pp. 868–869, 1997.

[82] J.-H. Baek, I. H. Choi, B. Lee, W. S. Han, and H. K. Cho, "Precise control of 1.55 μm vertical-cavity surface-emitting laser structure with InAlGaAs/InAlAs Bragg reflectors by *in situ* growth monitoring," *Applied Physics Letters*, vol. 75, no. 11, pp. 1500–1502, 1999.

[83] I. Sagnes, G. L. Roux, C. Mériadec, A. Mereuta, G. Saint-Girons, and M. Bensoussan, "MOCVD InP/AIGalnAs distributed Bragg reflector for 1.55 μm VCSELs," *IET Electronics Letters*, vol. 37, no. 8, pp. 500–501, 2001.

[84] N. Nishiyama, C. Caneau, B. Hall, G. Guryanov, M. H. Hu, X. S. Liu, M.-J. Li, R. Bhat, , and C. E. Zah, "Long-wavelength vertical-cavity surface-emitting lasers on InP with lattice matched AlGaInAs-InP DBR grown by MOCVD," *IEEE Journal of Selected Topics in Quantum Electronics*, vol. 11, no. 5, pp. 990–998, 2005.

[85] S. K. Y. Imajo, A. Kasukawa and H. Okamoto, "GaInAsP/InP semiconductor multilayer reflector grown by metalorganic chemical vapor deposition and its application to surface emitting laser," *Japanese Journal of Applied Physics*, vol. 29, pp. L1130–1132, 1990.

[86] I. F. L. Dias, B. Nabet, A. Kohl, J. L. Benchimol, and J. C. Harmand, "Electrical and optical characteristics of n-type-doped distributed Bragg mirrors on InP," *IEEE Photonics Technology Letters*, vol. 10, no. 6, pp. 763–765, 1998.

[87] B. Lambert, Y. Toudic, Y. Rouillard, M. Gauneau, M. Baudet, F. Alard, I. Valiente, and J. C. Simon, "High reflectivity 1.55 μm (Al)GaAsSb/AlAsSb Bragg reflector lattice matched on InP substrates," *Applied Physics Letters*, vol. 66, no. 4, pp. 442–444, 1995.

[88] A. Naka and S. Saito, "88°C, continuous-wave operation of apertured, intracavity contacted, 1.55 μm vertical-cavity surface-emitting lasers," *Applied Physics Letters*, vol. 78, no. 10, pp. 1337–1339, 2001.

[89] G. Almuneau, E. Hall, T. Mukaihara, S. Nakagawa, C. Luo, D. Clarke, and L. Coldren, "Improved electrical and thermal properties of InP-AlGaAsSb Bragg mir-

rors for long-wavelength vertical-cavity lasers," *IEEE Photonics Technology Letters*, vol. 12, no. 10, pp. 1322–1324, 2000.

[90] R. J. Ram, L. Yang, K. Nauka, Y. M. Houng, M. Ludowise, D. E. Mars, J. J. Dudley, and S. Y. Wang, "Analysis of wafer fusing for 1.3 μm vertical cavity surface emitting lasers," *Applied Physics Letters*, vol. 62, no. 20, pp. 2474–2476, 1993.

[91] A. Karim, P. Abraham, D. Lofgreen, Y.-J. Chiu, J. Piprek, and J. Bowers, "Wafer bonded 1.55 μm vertical-cavity lasers with continuous-wave operation up to 105 °C," *Applied Physics Letters*, vol. 78, no. 18, pp. 2632–2633, 2001.

[92] W.-J. Choi, P. D. Dapkus, and J. J. Jewell, "1.2 μm GaAsP/InGaAs strain compensated single-quantum-well diode laser on GaAs using metal-organic chemical vapor deposition," *IEEE Photonics Technology Letters*, vol. 11, no. 12, pp. 1572–1574, 1999.

[93] P. Sundgren, R. M. von Würtemberg, J. Berggren, M. Hammar, M. Ghisoni, V. Oscarsson, E. Ödling, and J. Malmquist, "High performance 1.55 μm vertical external cavity surface emitting laser with broadband integrated dielectric-metal mirror," *IET Electronics Letters*, vol. 39, no. 15, pp. 1128–1129, 2003.

[94] T. Anan, K. Nishi, S. Sugou, M. Yamada, K. Tokutome, and A. Gomyo, "GaAsSb: A novel material for 1.3 μm VCSELs," *IET Electronics Letters*, vol. 34, no. 22, pp. 2127–2128, 1998.

[95] T. Anan, M. Yamada, K. Nishi, K. Kurihara, K. Tokutome, A. Kamei, and S. Sugou, "Continuous-wave operation of 1.30 μm GaAsSb/GaAs VCSELs," *IET Electronics Letters*, vol. 37, no. 9, pp. 566–567, 2001.

[96] M. Kondow, T. Kitatani, S. Nakatsuka, M. C. Larson, K. Nakahara, Y. Yazawa, M. Okai, and K. Uomi, "GaInNAs: a novel material for long-wavelength semiconductor lasers," *IEEE Journal of Selected Topics in Quantum Electronics*, vol. 3, no. 3, pp. 719–730, 1997.

[97] G. Jaschke, R. Averbeck, L. Geelhaar, and H. Riechert, "Low threshold InGaAsN/GaAs lasers beyond 1500 nm," vol. 278, pp. 224–228, 2005.

[98] J. A. Lott, N. N. Ledentsov, V. M. Ustinov, N. A. Maleev, A. E. Zhukov, A. R. Kovsh, M. V. Maximov, B. V. Volovik, Z. I. Alferov, and D. Bimberg, "InAs-InGaAs quantum dot VCSELs on GaAs substrates emitting at 1.3 μm," *IET Electronics Letters*, vol. 36, no. 16, pp. 1384–1385, 2000.

[99] V. M. Ustinov, N. A. Maleev, A. R. Kovsh, and A. E. Zhukov, "Quantum dot VCSELs," *Physica Status Solidi (a)*, vol. 202, no. 3, pp. 396–402, 2005.

[100] X. Yang, M. J. Jurkovic, J. B. Heroux, and W. I. Wang, "Molecular beam epitaxial growth of InGaAsN:Sb/GaAs quantum wells for long-wavelength semiconductor lasers," *Applied Physics Letters*, vol. 75, no. 2, pp. 178–180, 1999.

[101] S. R. Bank, H. Bae, L. L. Goddard, H. B. Yuen, M. A. Wistey, R. Kudrawiec, and J. S. Harris Jr., "Recent progress on 1.55-μm dilute-nitride lasers," *IEEE Journal of Quantum Electronics*, vol. 43, no. 9, pp. 773–785, 2007.

[102] J. Konttinen, "Dilute nitride multi-quantum-well photonic structures," Ph.D. dissertation, Tampere University of Technology, Tampere, Finland, 2007.

[103] R. W. Boyd, *Nonlinear optics*, 2nd ed. San Diego, CA: Academic Press, 2003.

[104] O. Svelto, *Principles of Lasers*, 4th ed. New York, NY: Plenum Press, 1998.

[105] M. Rusu, "Frequency conversion using ultrafast fiber lasers," Ph.D. dissertation, Tampere University of Technology, Tampere, Finland, 2006.

[106] A. V. Smith, "SNLO nonlinear optics code version 40," Sandia National Laboratories, Albuquerque, NM 87185-1423. [Online]. Available: http://www.sandia.gov/imrl/XWEB1128/xxtal.htm

[107] "Nonlinear crystal specifications," Red Optronics. [Online]. Available: http://www.redoptronics.com/crystals.html

[108] P. S. Dutta, H. L. Bhat, and V. Kumar, "The physics and technology of gallium antimonide: An emerging optoelectronic material," *Journal of Applied Physics*, vol. 81, no. 1, pp. 5821–5870, 1997.

[109] F. K. Tittel, D. Richter, and A. Fried, "Mid-infrared laser applications in spectroscopy," Rice Quantum Institute, Rice University, Houston, TX 77251-1892, USA. [Online]. Available: http://www.ece.rice.edu/lasersci/Chapter%2011%20(Mid-IR%20laser%20applications%20in%20spectroscopy).pdf

[110] M. Rattunde, C. Mermelstein, J. Schmitz, R. Kiefer, W. Pletschen, M. Walther, and J. Wagner, "GaSb-based diode lasers for power applications in the 2 μm spectral range," in *Proc. Conference on Lasers and Electro-Optics Europe*, 2003, p. 142.

[111] H. K. Choi, J. N. Walpole, G. W. Turner, M. K. Connors, L. J. Missaggia, and M. J. Manfra, "GaInAsSb-AlGaAsSb tapered lasers emitting at 2.05 μm with 0.6-W diffraction-limited power," *IEEE Photonics Technology Letters*, vol. 10, no. 8, pp. 938–940, 1998.

[112] C. Pfahler, G. Kaufel, M. T. Kelemen, M. Mikulla, M. Rattunde, J. Schmitz, and J. Wagner, "GaSb-based tapered diode lasers at 1.93 μm with 1.5-W nearly diffraction-limited power," *IEEE Photonics Technology Letters*, vol. 18, no. 6, pp. 758–760, 2006.

[113] M. Hümmer, K. Rößner, T. Lehnhardt, M. Müller, A. Forchel, R. Werner, M. Fischer, and J. Koeth, "Long wavelength GaInAsSb-AlGaAsSb distributed-feedback lasers emitting at 2.84 μm," *IET Electronics Letters*, vol. 42, no. 10, pp. 583–584, 2006.

[114] J. Seufert, M. Fischer, M. Legge, J. Koeth, R. Werner, M. Kamp, and A. Forchel, "DFB laser diodes in the wavelength range from 760 nm to 2.5 μm," *Spectrochimica Acta Part A: Molecular and Biomolecular Spectroscopy*, vol. 60, no. 14, pp. 3243–3247, 2004.

[115] M. Müller, H. Scherer, T. Lehnhardt, K. Rößner, M. Hümmer, R. Werner, and A. Forchel, "Widely tunable coupled cavity lasers at 1.9 μm on GaSb," *IEEE Photonics Technology Letters*, vol. 19, no. 8, pp. 592–594, 2007.

[116] A. N. Baranov, Y. Rouillard, G. Boissier, P. Grech, S. Gaillard, and C. Alibert, "Sb-based monolithic VCSEL operating near 2.2 μm at room temperature," *Electronics Letters*, vol. 34, no. 3, pp. 281–282, 1998.

[117] A. Ouvrard, A. Garnache, L. Cerutti, F. Genty, and D. Romanini, "Single-frequency tunable Sb-based VCSELs emitting at 2.3 μm," *IEEE Photonics Technology Letters*, vol. 17, no. 10, pp. 2020–2022, 2005.

[118] L. Cerutti, A. Garnache, A. Ouvrard, and F. Genty, "High temperature continuous wave operation of Sb-based vertical external cavity surface emitting laser near 2.3 μm," *Journal of Crystal Growth*, vol. 268, no. 1-2, pp. 128–134, 2004.

[119] K. Kato, "Second-harmonic and sum-frequency generation to 4950 and 4589 Å in KTP," *IEEE Journal of Quantum Electronics*, vol. 24, no. 1, pp. 3–4, 1988.

[120] M. Whitehead and G. Parry, "Two-wavelength interferometer based on a two-color laser-diode array and the second-order correlation technique," *Optics Letters*, vol. 20, no. 9, pp. 1071–1073, 1995.

[121] K. Kato, "High-Power Difference-Frequency Generation at 5-11 μm in $AgGaS_2$," *IEEE Journal of Quantum Electronics*, vol. 20, no. 7, pp. 698–699, 1984.

[122] J. Faist, F. Capasso, D. L. Sivco, C. Sirtori, A. L. Hutchinson, and A. Y. Cho, "Quantum cascade laser," vol. 264, no. 5158, pp. 553–556, 1994.

[123] Y. Kimura and M. Nakazawa, "Multiwavelength cw laser oscillation in a Nd^{3+} and Er^{3+} doubly doped fiber laser," *Applied Physics Letters*, vol. 53, no. 14, pp. 1251–1253, 1998.

[124] J. Chow, G. Town, B. Eggleton, M. Ibsen, K. Sugden, and I. Bennion, "Multiwavelength generation in an Erbium-doped fiber laser using in-fiber comb filters," *IEEE Journal of Quantum Electronics*, vol. 8, no. 1, pp. 60–62, 1996.

[125] J. M. Battiato, T. F. Morse, and R. K. Kostuk, "Dual-wavelength common-cavity codoped fiber laser," *IEEE Photonics Technology Letters*, vol. 9, no. 7, pp. 913–915, 1997.

[126] C. Bethea, "Megawatt power at 1.318 μ in Nd^{3+}:YAG and simultaneous oscillation at both 1.06 and 1.318 μ," *IEEE Journal of Quantum Electronics*, vol. 9, no. 2, pp. 254–254, 1977.

[127] Y.-F. Chen, "cw dual-wavelength operation of a diode-end-pumped Nd:YVO_4 laser," *Applied Physics B*, vol. 70, pp. 475–478, 2000.

[128] I. H. White, K. O. Nyairo, P. A. Kirkby, and C. J. Armistead, "Demonstration of a $1\times$ 2 multichannel grating cavity laser forwavelength division multiplexing (WDM) application," *IET Electronics Letters*, vol. 26, no. 13, pp. 832–834, 1990.

[129] K. Poguntke, J. B. D. Soole, A. Scherer, H. P. LeBlance, C. Caneau, R. Baht, and M. A. Koza, "Simultaneous multiple wavelength operation of a multistripe array grating integrated cavity laser," *Applied Physics Letters*, vol. 62, no. 17, pp. 2024–2026, 1993.

[130] T. Hidaka and Y. Hatano, "Simultaneous two wave oscillation LD using biperiodic binary grating," *IET Electronics Letters*, vol. 27, no. 12, pp. 1075–1076, 1991.

[131] C.-F. Lin, M.-J. Chen, and B.-L. Lee, "Wide-range tunable dual-wavelength semiconductor laser using asymmetric dual quantum wells," *IEEE Photonics Technology Letters*, vol. 10, no. 9, pp. 1208–1210, 1998.

[132] P. Pellandini, R. Stanley, R. Houdre, U. Oesterle, and M. Ilegems, "Dual-wavelength laser emission from a coupled semiconductor microcavity," *Applied Physics Letters*, vol. 71, no. 7, pp. 864–866, 1997.

[133] T. Leinonen, S. Ranta, A. Laakso, Y. Morozov, M. Saarinen, and M. Pessa, "Dual-wavelength generation by vertical external cavity surface-emitting laser," *Optics Express*, vol. 15, no. 20, pp. 13 451–13 456, 2007.